Correspondence to:

M. Kruglyakov,
m.kruglyakov@gmail.com

A Proper Use of the Adjacent Land-Based Observatory Magnetic Field Data to Account for the Geomagnetic Disturbances During Offshore Directional Drilling

Mikhail Kruglyakov[1] [ID]**, Alexey Kuvshinov[2]** [ID]**, and Manoj Nair[3,4]**

[1]University of Otago, Dunedin, New Zealand, [2]Institute of Geophysics, ETH Zürich, Zurich, Switzerland, [3]Cooperative Institute for Research in Environmental Sciences, University of Colorado, Boulder, CO, USA, [4]National Centers for Environmental Information, NOAA, Boulder, CO, USA

Abstract Directional drilling in the oil fields relies particularly on the "on-fly" measurements of the natural magnetic field (measurements while drilling; MWD); the MWD are eventually used to construct the well path. These measurements are the superposition of the signals from the internal, core and crustal, and external, ionospheric and magnetospheric sources and the noise from magnetic elements in the borehole assembly. The internal signals are mostly constant in time and accounted for through the Earth's internal field models. The signals of external origin give rise to diurnal and irregular spatio-temporal magnetic field variations observable in the MWD. One of the common ways to mitigate the effects of these variations in the MWD is to correct readings for the data from an adjacent land-based magnetic observatory/site. This method assumes that the land-based signals are similar to those at the seabed drilling site. In this paper, we show that the sea level and seabed horizontal magnetic fields differ significantly, reaching up to 30% of sea level values in many oceanic regions. We made this inference from the global forward modeling of the magnetic field using realistic models of conducting Earth and time-varying sources. To perform such modeling, we elaborated a numerical approach to efficiently calculate the spatio-temporal evolution of the magnetic field. Finally, we propose and validate a formalism allowing researchers to obtain trustworthy seabed signals using measurements at the adjacent land-based site and exploiting the modeling results, thus without needing additional measurements at the seabed site.

Plain Language Summary Knowing the position of existing and new oil wells is vital for economic and safe sub-horizontal drilling operations. A lower uncertainty in well positions allows for hitting smaller targets and avoiding the risk of well collisions. Determining the well position relies particularly on magnetic sensors installed close to the drill bit. For this, the models of spatially variable but constant in time magnetic field in the region of interest are routinely used. However, spatially and temporally varying space-weather-related geomagnetic field disturbances may affect the accuracy of the well position. One of the common ways to mitigate this problem is to correct magnetic field readings at a drill bit for the magnetic field measurements from an adjacent land-based magnetic observatory. However, this method assumes that the land-based signals are similar to those at the seabed drilling site. In this paper, we show that this is not the case, that is, the sea level and seabed magnetic fields differ significantly due to the electrical conductivity of the seawater column above the seabed site. Moreover, we propose and justify a numerical scheme which allows researchers to obtain trustworthy seabed signals by still using land-based data but exploiting the results of dedicated modeling.

1. Introduction

Modern directional drillers primarily rely on natural magnetic and gravitational fields to determine the orientation of their borehole assembly (BHA). This is because the GPS signals do not penetrate the underground. Ruggedized versions of vector magnetometers and accelerometers installed in the BHA measure the magnetic and gravity fields at fixed intervals when the drilling is stopped. This process is called "Measurement While Drilling (MWD)." The MWD data are transmitted to the drilling surface via mud pulses through the drilling fluid. By combining the magnetic and accelerometer data, the drilling engineers determine the orientation of the BHA. By combining the distance drilled with the orientation information, they construct the well path of the borehole within an envelope of uncertainty. However, the magnetometers only provide the azimuth of the BHA with respect to the local magnetic field's horizontal direction. Hence, properly converting the magnetic measurements

to geographic orientation using a geomagnetic field model is imperative. At the site of the borehole, the local magnetic field is the superposition of magnetic fields primarily arising from the following natural sources: Earth's core, crust and space-weather-related electric currents in the magnetosphere and ionosphere. Note that the MWD data might also be influenced by the magnetic signals arising from the BHA. The so-called "drillstring interference" is mitigated by additional processing such as multi-station analysis (e.g., Buchanan et al. (2013)) or by using tools manufactured with nonmagnetic materials. The core and crustal fields (being mostly static) can be accounted for through high-resolution models of the Earth's internal field, such as the High Definition Geomagnetic Model (Nair et al., 2021) and British Geological Survey Global Geomagnetic Model (Beggan et al., 2021). However, electric currents in the ionosphere and magnetosphere and their counterparts induced in the conducting Earth give rise to diurnal and irregular variations observable in the MWD. One of the common ways for MWD engineers to mitigate the space-weather effects is to correct MWD readings for the magnetic field data from an adjacent land-based observatory or by interpolating the magnetic variations between a group of adjacent, land-based observatories (Reay et al., 2005). Poedjono et al. (2015) proposed sea level magnetic measurements using autonomous marine vehicles to support offshore drilling. Both of these methods assume that the signals measured at the sea level are similar to those at the seabed drilling site. Based on electromagnetic (EM) modeling, this paper shows that such approximations cannot be used for an offshore site. The EM induction causes the sea level and seabed magnetic fields to differ significantly at the same lateral location (i.e., at the same geographic latitude and longitude of the sea level and seabed points). Moreover, we propose and verify a numerical formalism allowing researchers to obtain trustworthy seabed signals using magnetic field measurements at the adjacent land-based site and magnetic fields modeled at land-based and seabed sites.

The paper is organized as follows. Section 2 discusses a methodology allowing us to calculate accurately and efficiently time-varying magnetic field in a given conductivity model of the Earth, provided a source of magnetic field variations is also known. The methodology—being general, particularly in terms of the source parameterization—is implemented in this paper to model and analyze the spatio-temporal evolution of the magnetic field during geomagnetic storms. Global-scale problem setup advocates the parameterization of the magnetospheric source responsible for the storms using spherical harmonics (SH). Estimation of the corresponding expansion coefficients from hourly-mean observatory data is also discussed in Section 2. Note that using a large-scale source model represented by SH and temporally resolved with a relatively low sampling interval (1 hr) precludes analysis of the high-latitude signals originating from an auroral ionospheric source, typically much smaller-scale and highly variable in time. Section 3 presents results of time-domain modeling of the magnetic field at sea level and seabed during the storms. Modeling is performed using three-dimensional (3-D) conductivity and (data-based) source models built as realistic as feasible. Section 3 demonstrates that the sea level horizontal magnetic fields significantly differ from those at the seabed, especially during the main phase of the geomagnetic storms; recall that conventionally they are assumed to be the same in MWD applications. Section 4 compares modeling results with observations at land-based and seabed sites. Further, Section 5 introduces and justifies a scheme to obtain the seabed signals using the data from the adjacent land-based observatory and the results of comprehensive modeling discussed in Section 3. A scheme exploits a concept of transfer functions (TFs) that relate—in frequency domain—three components of the magnetic field at the seabed site of interest with those at the adjacent land-based site. In an example of the seabed observations in the Philippine Sea, we demonstrate the workability of the proposed scheme. Finally, Section 6 summarizes our findings and outlines the paths for further research. The paper also includes three appendices detailing the theoretical results presented in the main text.

2. Methodology

2.1. Governing Equations for Magnetic Field in the Frequency Domain

We start with the discussion of the problem in the frequency domain. Maxwell's equations govern EM field variations and, in the frequency domain, these equations read as

$$\frac{1}{\mu_0} \nabla \times \mathbf{B} = \sigma \mathbf{E} + \mathbf{j}^{\text{ext}}, \tag{1}$$

$$\nabla \times \mathbf{E} = i\omega \mathbf{B}, \tag{2}$$

where μ_0 is the magnetic permeability of free space, ω is angular frequency, $\mathbf{j}^{\text{ext}}(\mathbf{r}, \omega)$ is the extraneous (inducing) electric current density, $\mathbf{B}(\mathbf{r}, \omega; \sigma)$ and $\mathbf{E}(\mathbf{r}, \omega; \sigma)$ are magnetic and electric fields, respectively. $\sigma(\mathbf{r})$ is the spatial distribution of electrical conductivity, $\mathbf{r} = (r, \theta, \varphi)$ a position vector, in our case in the spherical geometry. Note that we neglected displacement currents and adopted the following Fourier convention

$$f(t) = \frac{1}{2\pi} \int_{-\infty}^{\infty} f(\omega) e^{-i\omega t} d\omega. \tag{3}$$

We will assume that the current density, $\mathbf{j}^{\text{ext}}(\mathbf{r}, \omega)$, can be represented as a linear combination of spatial modes $\mathbf{j}_i(\mathbf{r})$

$$\mathbf{j}^{\text{ext}}(\mathbf{r}, \omega) = \sum_{i=1}^{L} c_i(\omega) \mathbf{j}_i(\mathbf{r}). \tag{4}$$

The form of spatial modes $\mathbf{j}_i(\mathbf{r})$ (and their number, L) varies with application. For example, $\mathbf{j}^{\text{ext}}(\mathbf{r}, \omega)$ is parameterized via SH in Püthe and Kuvshinov (2013), Honkonen et al. (2018), Guzavina et al. (2019), Grayver et al. (2021), current loops in Sun and Egbert (2012), eigenmodes from the Principal Component Analysis (PCA) of the physics-based models in Egbert et al. (2021) and Zenhausern et al. (2021), and eigenmodes from the PCA of the data-based models in Kruglyakov et al. (2022). In this paper—because we work on a whole sphere—we will use SH parameterization of the source, namely

$$\mathbf{j}^{\text{ext}}(\mathbf{r}, \omega) = \sum_{l,m} \epsilon_l^m(\omega) \mathbf{j}_l^m(\mathbf{r}), \tag{5}$$

where l and m are degree and order of SH, respectively, expression $\sum_{l,m}$ stands for the following double sum

$$\sum_{l,m} \equiv \sum_{l=1}^{N_l} \sum_{m=-l}^{l}, \tag{6}$$

and $\mathbf{j}_l^m(\mathbf{r})$ is the (extraneous) source corresponding to a specific SH, namely (see Kuvshinov et al. (2021))

$$\mathbf{j}_l^m(\mathbf{r}) = \delta(r - a+) \frac{1}{\mu_0} \frac{2l+1}{l+1} \mathbf{e}_r \times \nabla_{\perp} Y_l^m(\theta, \varphi), \tag{7}$$

where δ is Dirac's delta function, a is the mean radius of the Earth, $a+$ means that $\mathbf{j}_l^m$ flows above the Earth' surface, $\mathbf{e}_r$ is radial unit vector of the spherical coordinate system, $\nabla_{\perp} = r\nabla_H$, ∇_H is tangential part of gradient, $Y_l^m(\vartheta, \varphi) = P_l^{|m|}(\cos \theta) e^{im\varphi}$ with $P_l^{|m|}$ given by the Schmidt quasi-normalized associated Legendre functions.

By virtue of the linearity of Maxwell's equations with respect to the $\mathbf{j}^{\text{ext}}(\mathbf{r}, \omega)$ term, we can expand the total (i.e., inducing plus induced) magnetic field as a linear combination of individual fields $\mathbf{B}_l^m$,

$$\mathbf{B}(\mathbf{r}, \omega; \sigma) = \sum_{l,m} \epsilon_l^m(\omega) \mathbf{B}_l^m(\mathbf{r}, \omega; \sigma), \tag{8}$$

where the $\mathbf{B}_l^m(\mathbf{r}, \omega; \sigma)$ field is the "magnetic" solution of corresponding Maxwell's equations; see Equations 1 and 2 with the extraneous source in the form of $\mathbf{j}_l^m(\mathbf{r})$.

2.2. Governing Equations for Magnetic Field in the Time Domain

The transformation of the Equation 8 into the time domain leads to the representation of the magnetic field as

$$\mathbf{B}(\mathbf{r}, t; \sigma) = \sum_{l,m} \int_0^{\infty} \epsilon_l^m(t - \tau) \mathbf{B}_l^m(\mathbf{r}, \tau; \sigma) d\tau. \tag{9}$$

The reader is referred to Appendix A in Kruglyakov et al. (2022) for more details on the convolution integrals in the latter equation. We note that we use the same notation for the fields in the time and frequency domain. Equation 9 shows how magnetic field can be calculated provided ϵ_l^m and conductivity model σ are given. To make

the formula ready for implementation, one also needs to estimate an upper limit of integrals in Equation 9, or, in other words, to evaluate a time interval, T, above which $\mathbf{B}_l^m(\mathbf{r}, \tau; \sigma)$ becomes negligibly small. The latter will allow us to rewrite Equation 9 as

$$\mathbf{B}(\mathbf{r}, t; \sigma) \approx \sum_{l,m} \int_0^T \epsilon_l^m(t - \tau) \mathbf{B}_l^m(\mathbf{r}, \tau; \sigma) d\tau. \tag{10}$$

Note that the upper limit in the integrals could be different for different $\mathbf{j}_l^m$, different components of the field, and different locations. However, we choose a conservative approach, taking a single T as a maximum from all individual upper limit estimates. Our model experiments (not shown in the paper) advocate that T should be taken as half a year.

The details of numerical calculation of the integrals in Equation 10 are presented in Appendix A. In short, assuming that $\epsilon_l^m(t)$ are given time series with the sampling interval Δt and $T = N_t \Delta t$, one calculates $\mathbf{B}(\mathbf{r}, t_k; \sigma)$ at $t_k = k\Delta t$ as

$$\mathbf{B}(\mathbf{r}, t_k; \sigma) \approx \sum_{l,m} \sum_{n=0}^{N_t} \epsilon_l^m(t_k - n\Delta t) \mathcal{M}_{\mathbf{B}_l^m}^n(\mathbf{r}, T; \sigma). \tag{11}$$

A few comments are relevant at this point.

- Quantities $\mathcal{M}_{\mathbf{B}_l^m}^n(\mathbf{r}, T; \sigma)$ are time-invariant, and—for the predefined set of $\mathbf{j}_l^m$ and a given conductivity model—are calculated only once, then stored and used, when the calculation of $\mathbf{B}(\mathbf{r}, t_k; \sigma)$ is required. Actual form and estimation of $\mathcal{M}_{\mathbf{B}_l^m}^n(\mathbf{r}, T; \sigma)$ are discussed in Appendix A.
- $\mathbf{r}$ stands for any location, thus allowing us to calculate magnetic field at satellite altitude, ground or/and seabed.
- Calculation of $\mathbf{B}(\mathbf{r}, t_k; \sigma)$ requires knowledge ϵ_l^m. We discuss a numerical scheme to estimate of ϵ_l^m in Section 2.3 and their actual estimation in Section 3.2.

2.3. A Numerical Scheme to Estimate ϵ_l^m From Observatory Data

A numerical scheme for estimating ϵ_l^m from observatory data relies on the following assumptions:

- The conductivity model—as realistic as possible—is known to us;
- We work with time series of three components of the magnetic field $\mathbf{B}$ at J geomagnetic observatories with coordinates $\mathbf{r}_j = (a, \theta_j, \varphi_j)$, $j = 1, 2, \ldots, J$. The time series are given with a sampling interval, Δt, which we take as 1 hr, meaning that we will work with hourly-mean observatory data.
- The above-mentioned time series are available for several years of observations, thus at time instants t_1, $t_1 + \Delta t$, $t_1 + 2\Delta t$, ...

With these assumptions in mind, the calculation of ϵ_l^m at a given time instant $t_k = k\Delta t$, $k = 1, 2, \ldots$ is performed as follows. Substituting coordinates of observatories into Equation 11 and rearranging the terms, we obtain a system of equations to determine $\epsilon_l^m(t_k)$

$$\sum_{l,m} \epsilon_l^m(t_k) \mathcal{M}_{\mathbf{B}_l^m}^0(\mathbf{r}_j, T; \sigma) = \mathbf{B}(\mathbf{r}_j, t_k) - \sum_{l,m} \sum_{n=1}^{N_t} \epsilon_l^m(t_k - n\Delta t) \mathcal{M}_{\mathbf{B}_l^m}^n(\mathbf{r}_j, T; \sigma), \quad j = 1, 2, \ldots, J. \tag{12}$$

As we discussed earlier, with T as long as a half of a year, $N_t \approx 24 \times 180 = 4{,}320$ provided sampling rate Δt is one hour. If we start with the first time instant, that is, with $t_k = t_1$ we do not have ϵ_l^m in the past; thus actual implementation of Equation 12 requires modification of it's right-hand side as

$$\sum_{l,m} \epsilon_l^m(t_k) \mathcal{M}_{\mathbf{B}_l^m}^0(\mathbf{r}_j, T; \sigma) = \mathbf{B}(\mathbf{r}_j, t_k) - \sum_{l,m} \sum_{n=1}^{\min(k-1, N_t)} \epsilon_l^m(t_k - n\Delta t) \mathcal{M}_{\mathbf{B}_l^m}^n(\mathbf{r}_j, T; \sigma). \tag{13}$$

Our model experiments (not shown in the paper) suggest that after a half of year (i.e., for $t'_k = (N_t + k)\, \Delta t$, $k = 1, 2, \ldots$) one obtains correct ϵ_l^m.

The expression (13) represents a system of linear equations (SLE) which is overdetermined when the number of unknowns (coefficients), $N_c = N_l \times (N_l + 2)$, is smaller than the number of equations, $N_o = N_b \times J$, where N_b stands for number of magnetic field components. In practice N_c (with $N_l = 4$ giving $N_c = 24$) is always much smaller than N_o (with J near 70 and $N_b = 2$ giving $N_o = 140$). $N_b = 2$ means we use two horizontal magnetic field components (assuming a prior Earth's conductivity model) to estimate ϵ_l^m. We only use the horizontal components since 3-D conductivity effects influence these components much less than the radial component (Kuvshinov, 2008). Note that the choice $N_l = 4$ allows us to represent both magnetospheric and a major part of the mid-latitude quasi-periodic (with period of 24 hr) ionospheric source.

Once $\epsilon_l^m\left(t'_k\right)$ are estimated for $t'_k = (N_t + k)\,\Delta t$, $k = 1, 2, \ldots$, one can calculate $\mathbf{B}(\mathbf{r}, t_k; \sigma)$, $k \geq 2N_t$ using Equation 11 at any location $\mathbf{r}$. In our modeling studies to be discussed in the following sections, $\mathbf{r}$ is either a laterally-uniform grid at the surface of the Earth (i.e., sea level) and at the seabed or coordinates of the land-based and seabed sites at which we analyze modeled and experimental results.

3. Modeling Results

3.1. Building the Conductivity Model

We build the 3-D conductivity model of the Earth, which includes nonuniform oceans and continents (generally with 3-D conductivity distribution) and a laterally uniform (1-D) mantle underneath. In this paper, we work with hourly-mean observatory data, which, in particular, means that we are forced to analyze magnetic field variations with periods of 2 hr and longer due to the Nyquist-Shannon theorem. For typical values of the Earth's conductivity, the penetration depth of the EM field exceeds a hundred kilometers (even at a period of 2 hr), much larger than the maximum ocean depths and sediment thicknesses (23 km). This fact allows us to shrink the nonuniform layer comprising oceans and continents into a thin shell of laterally-variable conductance (depth-integrated conductivity, with the depth taken as 23 km as mentioned earlier); discussion on the adequacy of the thin shell model can be found in Ivannikova et al. (2018).

For the conductance distribution in oceanic regions, we used $0.1° \times 0.1°$ marine map of conductance built by Grayver (2021). The inland conductances are obtained from the global conductivity model of Alekseev et al. (2015) which has a lateral resolution of $0.25° \times 0.25°$; to make it compatible with oceanic conductances, the resulting inland conductances were interpolated to $0.1° \times 0.1°$ grid. The inland conductance distribution was updated in North America using the recently published contiguous 3-D conductivity model of US (Kelbert et al., 2019). Figure 1 shows the global distribution of the compiled conductance. As for the 1-D structure underneath, it is taken from Kuvshinov et al. (2021).

3.2. Estimating ϵ_l^m

As discussed in Section 2.3, the estimation of ϵ_l^m requires the data from a global network of geomagnetic observatories. We work with 1997–2019 collection of hourly mean time series of the geomagnetic field from equatorward of $\pm 55°$ observatories. These data were retrieved from the British Geological Survey database (Macmillan & Olsen, 2013). The locations of observatories from which the data were used are shown in Figure 2. We then removed from the data the main field and its secular variations using the CHAOS model (Finlay et al., 2020).

Further, we solved overdetermined system of linear Equation 13 to obtain coefficients ϵ_l^m at each time instant t_k (t_1 stands for 1 January 1997 00:30:00 UTC) taking $N_l = 4$ in Equation 6, which gives us $N_c = N_l \times (N_l + 2) = 24$ coefficients per time instant. As mentioned in the previous section, we use only horizontal components of the magnetic field to estimate the coefficients.

We also note that since we consider the long (1997–2019) time series of the magnetic field, we adopt a geographic coordinate system—instead of the usually used geomagnetic coordinates—to avoid possible complications associated with the change of location of the geomagnetic pole during the considered (long) period of time.

During the observational period of 1997–2019, the number of observatories J in Equation 13 available at any time varied in the range from 38 to 112 due to the data gaps at specific observatories.
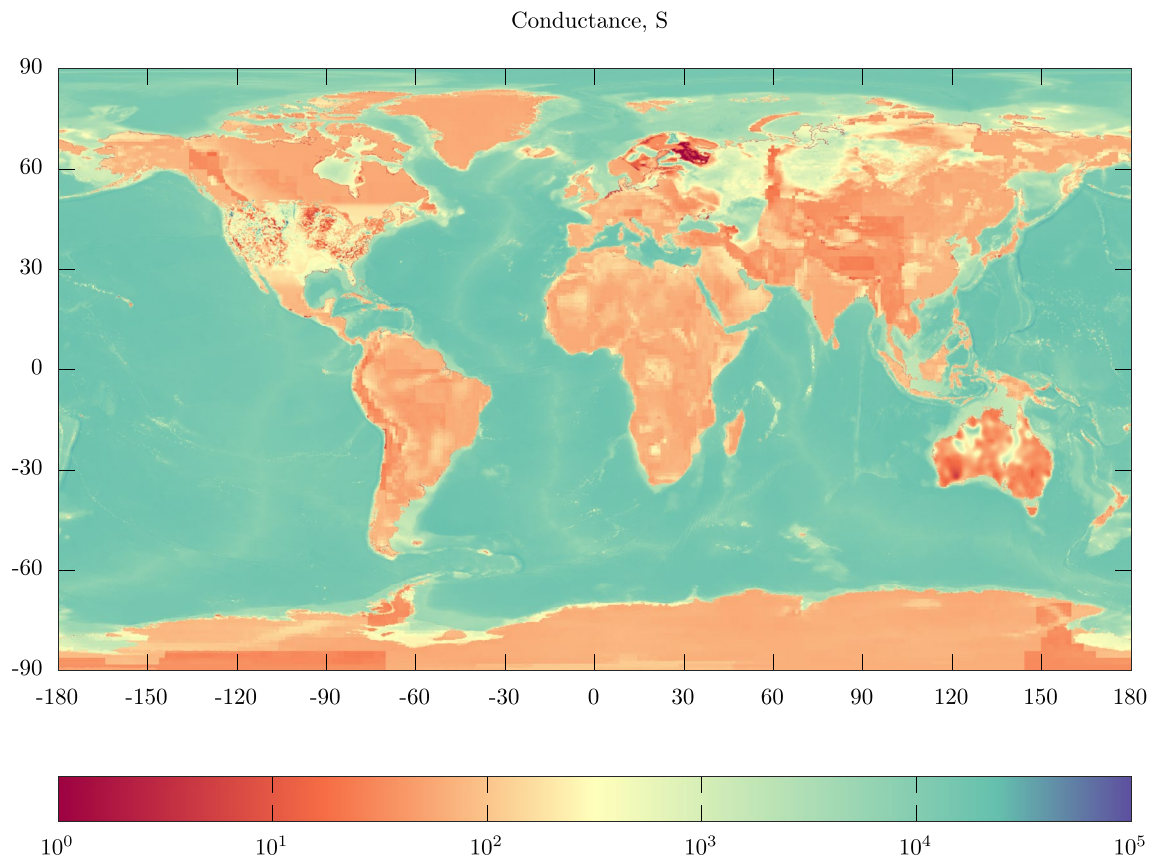
Conductance, S

Figure 1. Global conductance distribution in the surface thin shell (in Siemens). See details in the text.
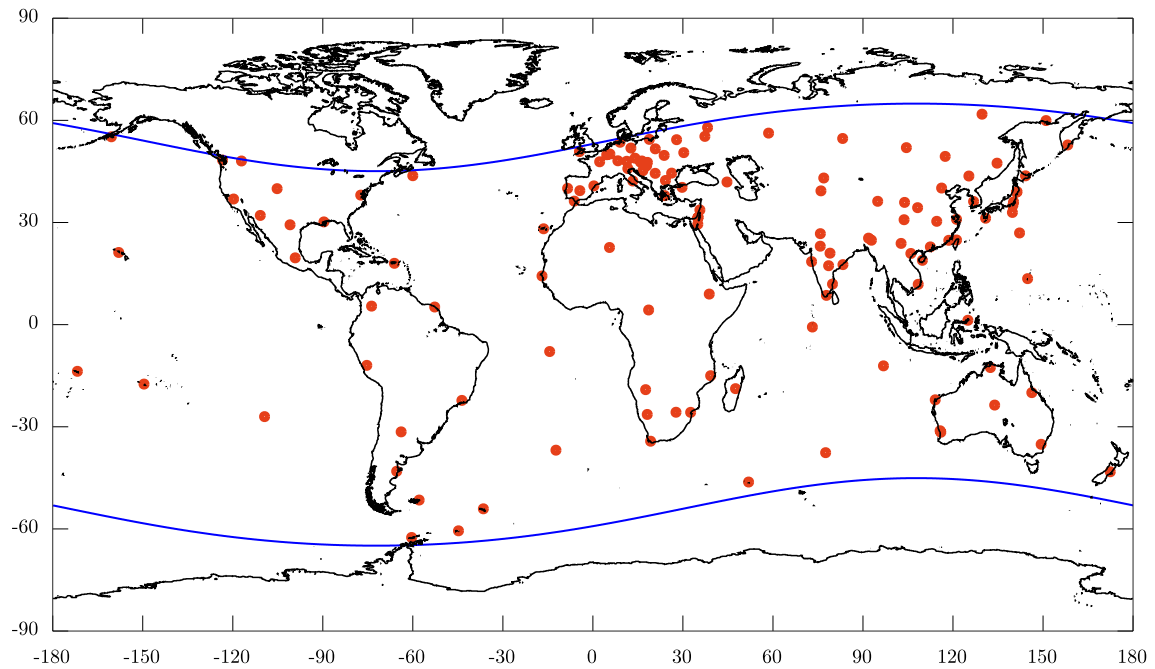
Figure 2. Locations of the observatories (red circles) from which data were used to estimate ϵ_l^m. Blue lines stand for $\pm 55°$ geomagnetic latitudes.
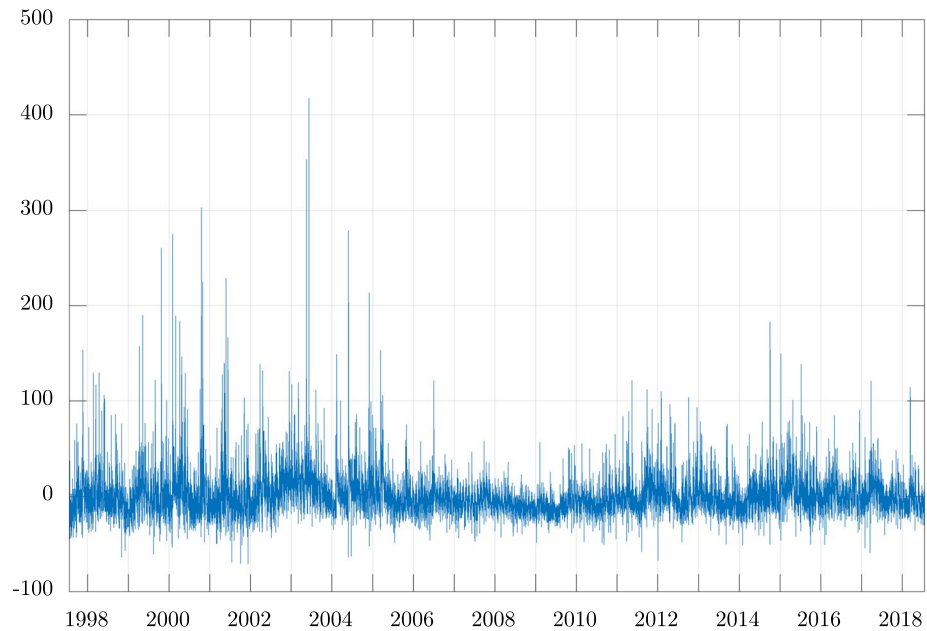
Figure 3. Time series of ϵ_1^0 estimated for 1998–2019 years. Ticks for the years stand for June 15 of the corresponding year.
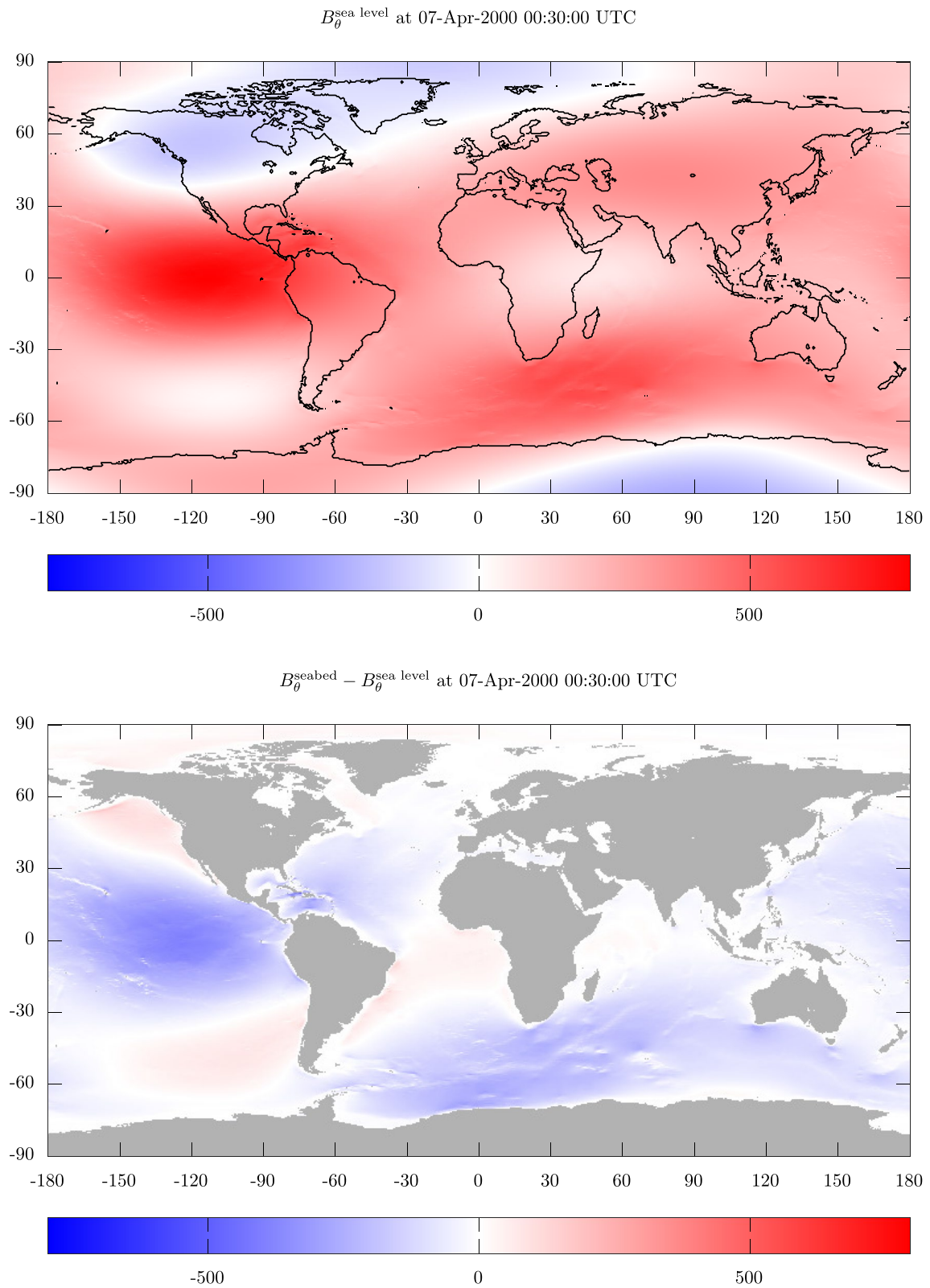
Final comment of this section refers to computation of $\mathcal{M}_{\mathbf{B}_l^m}^n(\mathbf{r}_j, T; \sigma)$. As shown in Appendix A it requires calculation of $\mathbf{B}_l^m(\mathbf{r}_j, \omega; \sigma)$ at a number of frequencies. Such calculations are performed by novel, accurate and efficient solver GEMMIE (Kruglyakov & Kuvshinov, 2022) which is based on an integral equation approach with contracting kernel (Pankratov & Kuvshinov, 2016). Constructively, $\mathbf{B}_l^m(\mathbf{r}, \omega; \sigma)$ are calculated on a lateral grid $0.1° \times 0.1°$ (in 3-D model discussed in Section 3.1) and then the results are interpolated to the observatory locations $\mathbf{r}_j$.

As an example, Figure 3 shows the time series of the dominant coefficient ϵ_1^0 estimated for 1998–2019. As expected, the time series is most disturbed in 1999–2003 (Solar Cycle No 23), the years of maximum solar activity in its 11-year cycle.

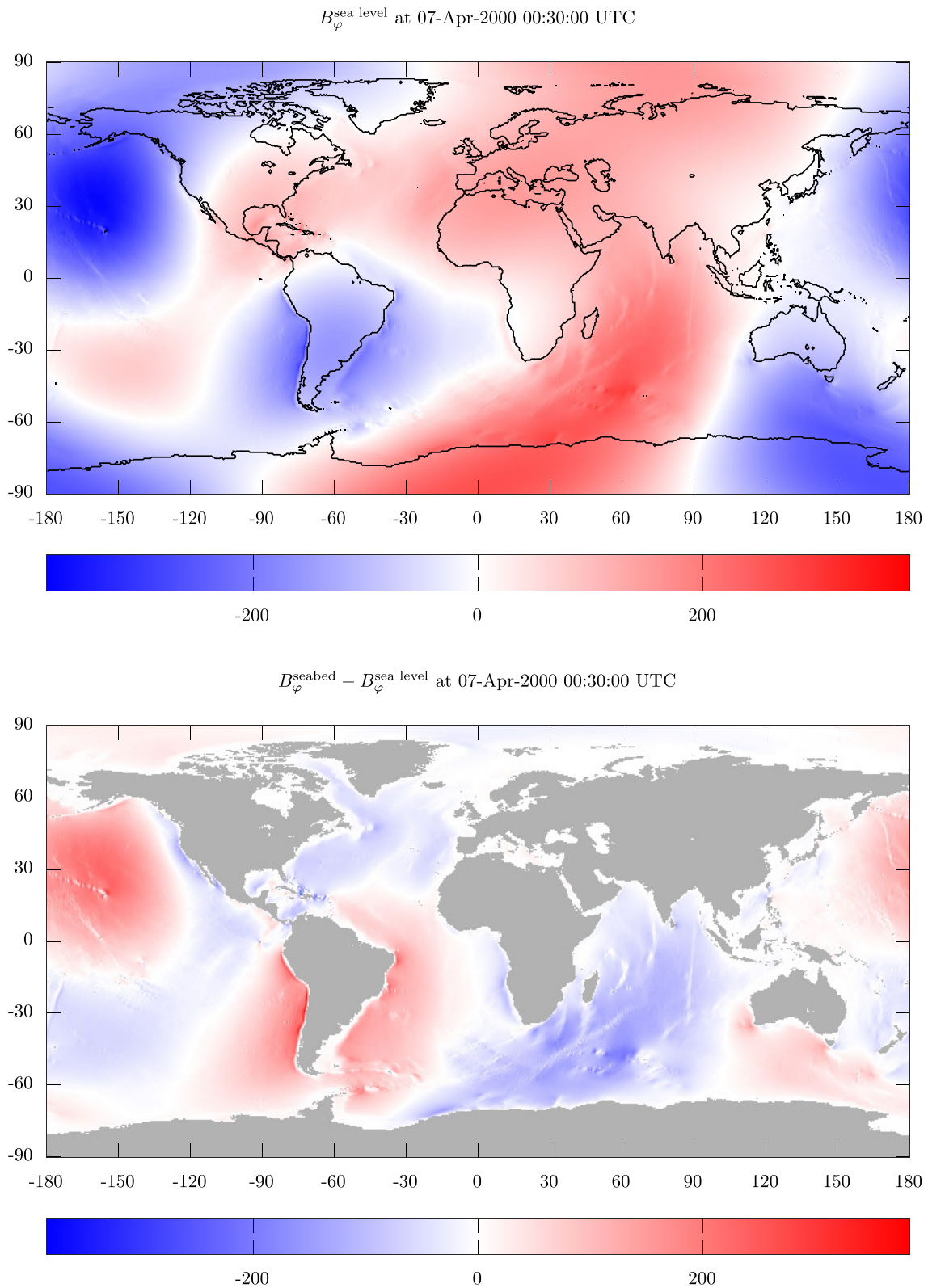### 3.3. Sea Level Versus Seabed Modeled Results

After estimating the time series of coefficients ϵ_l^m with one hour sampling interval for the 1998–2019 period, we calculate for the same period and with the same sampling interval the time series of the magnetic field at $0.1° \times 0.1°$ grid—both at sea level and seabed—using Equation 11. Note that 1997 year is not included into further analysis due to the reason, discussed in the Section 2.3 (see explanation after Equation 13). Having modeling results for the 1998–2019 years on the $0.1° \times 0.1°$ grid allows us to compare sea level and seabed magnetic fields globally or at specific locations for any time instant of the 1998–2019 period.

This section presents the global scale results during the main phase of three major geomagnetic storms. The main phase (centered around the peak of the geomagnetic storm) is chosen because the magnitude of the magnetic field reaches its maximum. Moreover, during the main phase, the field has the most complex spatial structure due to the enhanced asymmetry of the magnetospheric ring current, which is the primary source of geomagnetic storm signals. The Figures 4–9 present horizontal magnetic field, $\mathbf{B}_H = (B_\theta, B_\varphi)$, at sea level and corresponding differences between seabed and sea level results, $d\mathbf{B}_H = \mathbf{B}_H^{\text{seabed}} - \mathbf{B}_H^{\text{sea level}}$, during main phase of the storms: 7 April 2000, 30 October 2003 (Halloween storm) and 17 March 2015 (St. Patrick storm). The first storm is chosen because we have seabed data for it (see Section 4). Note also that we do not show the radial component since it remains continuous across the ocean column for the considered variations (with periods of 2 hr and longer). One can see that the difference reaches 25%–30% of sea level values in many oceanic regions, both in B_θ and B_φ components. Their difference generally depends on the ocean's depth, but this can be complicated by the spatial structure of the current sources. It is also seen that the spatial patterns of $\mathbf{B}_H$ and $d\mathbf{B}_H$ differ from storm to storm;

$B_\theta^{\text{sea level}}$ at 07-Apr-2000 00:30:00 UTC

$B_\theta^{\text{seabed}} - B_\theta^{\text{sea level}}$ at 07-Apr-2000 00:30:00 UTC

Figure 4. Modeled $B_\theta^{\text{sea level}}$ (top) and $B_\theta^{\text{seabed}} - B_\theta^{\text{sea level}}$ (bottom) at 00:30 7 April 2000 UTC. The results are in nT.

$B_\varphi^{\text{sea level}}$ at 07-Apr-2000 00:30:00 UTC

$B_\varphi^{\text{seabed}} - B_\varphi^{\text{sea level}}$ at 07-Apr-2000 00:30:00 UTC

Figure 5. Modeled $B_\varphi^{\text{sea level}}$ (top) and $B_\varphi^{\text{seabed}} - B_\varphi^{\text{sea level}}$ (bottom) at 00:30 7 April 2000 UTC. The results are in nT.

$B_\theta^{\text{sea level}}$ at 30-Oct-2003 20:30:00 UTC

$B_\theta^{\text{seabed}} - B_\theta^{\text{sea level}}$ at 30-Oct-2003 20:30:00 UTC
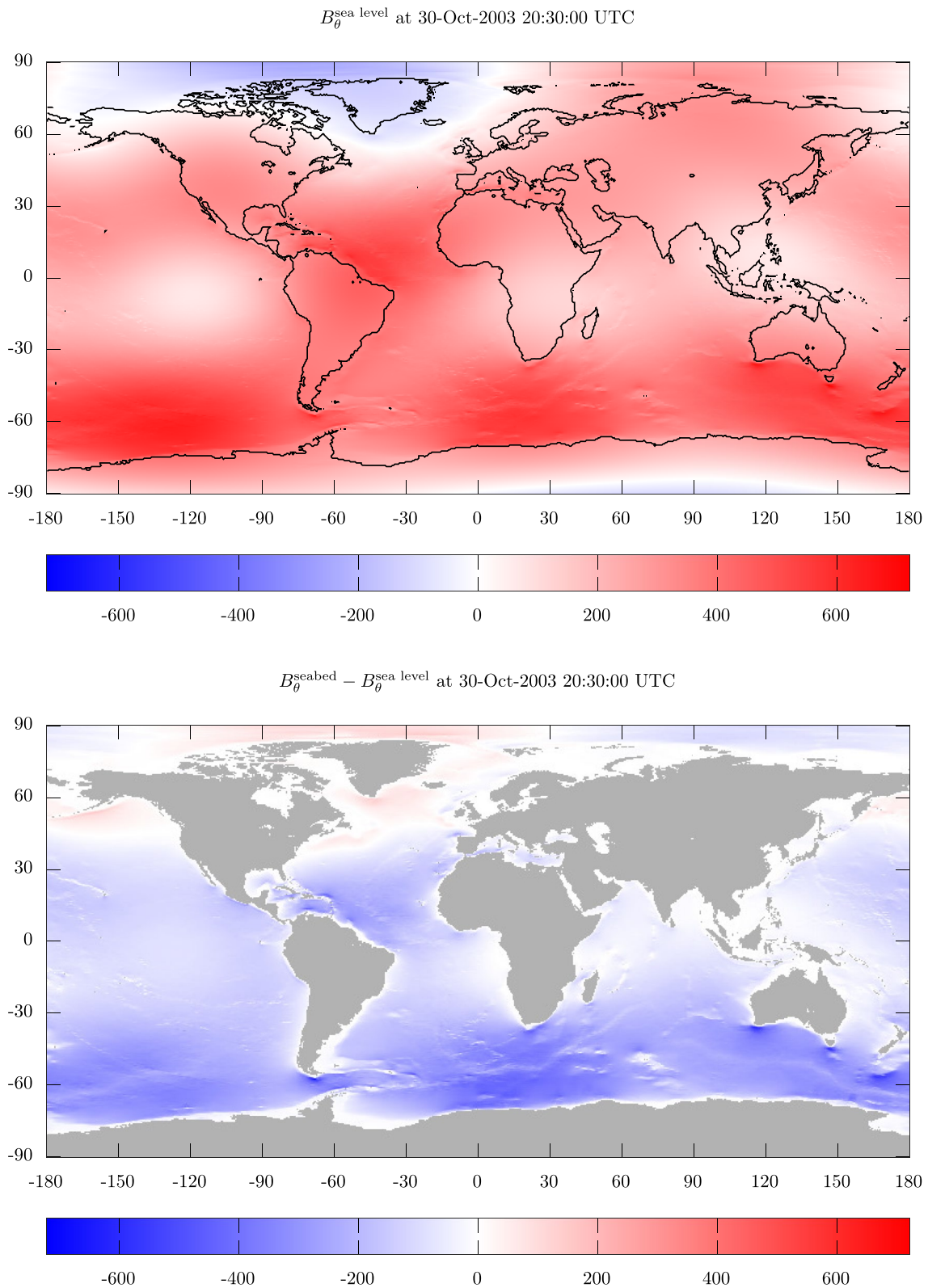
Figure 6. Modeled $B_\theta^{\text{sea level}}$ (top) and $B_\theta^{\text{seabed}} - B_\theta^{\text{sea level}}$ (bottom) at 20:30 30 October 2003 UTC (Halloween storm). The results are in nT.

$B_\varphi^{\text{sea level}}$ at 30-Oct-2003 20:30:00 UTC

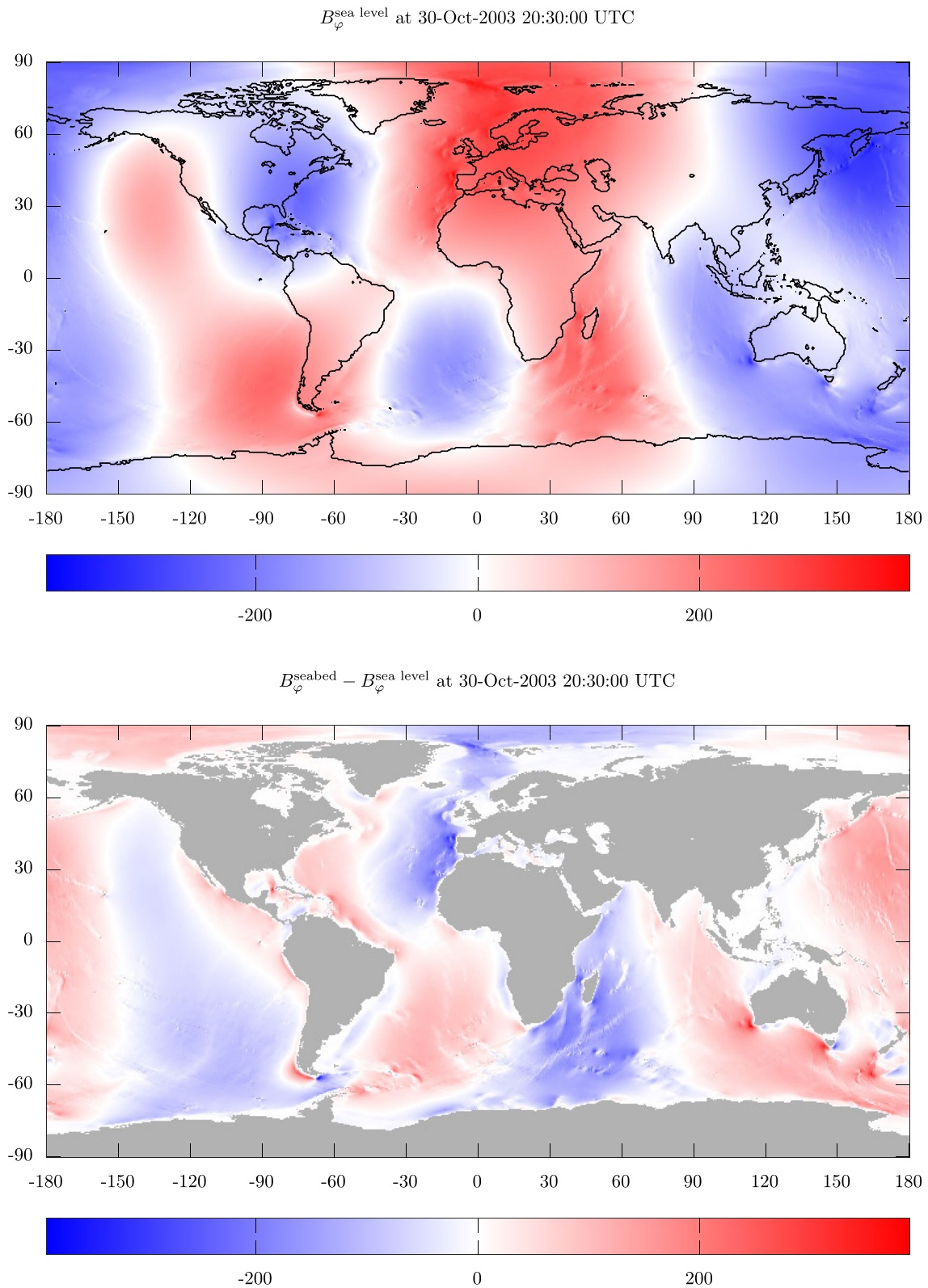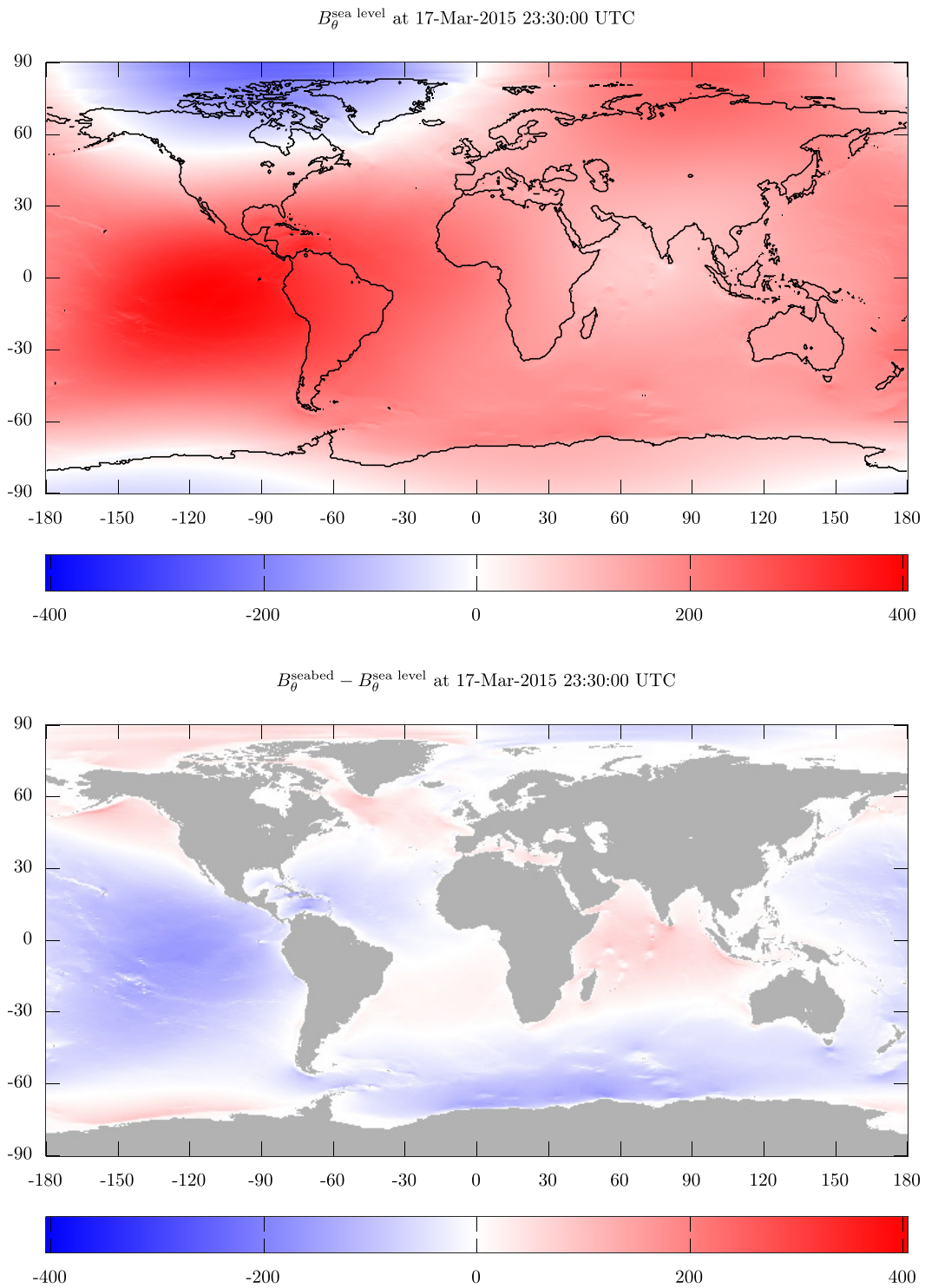$B_\varphi^{\text{seabed}} - B_\varphi^{\text{sea level}}$ at 30-Oct-2003 20:30:00 UTC

Figure 7. Modeled $B_\varphi^{\text{sea level}}$ (top) and $B_\varphi^{\text{seabed}} - B_\varphi^{\text{sea level}}$ (bottom) at 20:30 30 October 2003 UTC (Halloween storm). The results are in nT.

$B_\theta^{\text{sea level}}$ at 17-Mar-2015 23:30:00 UTC

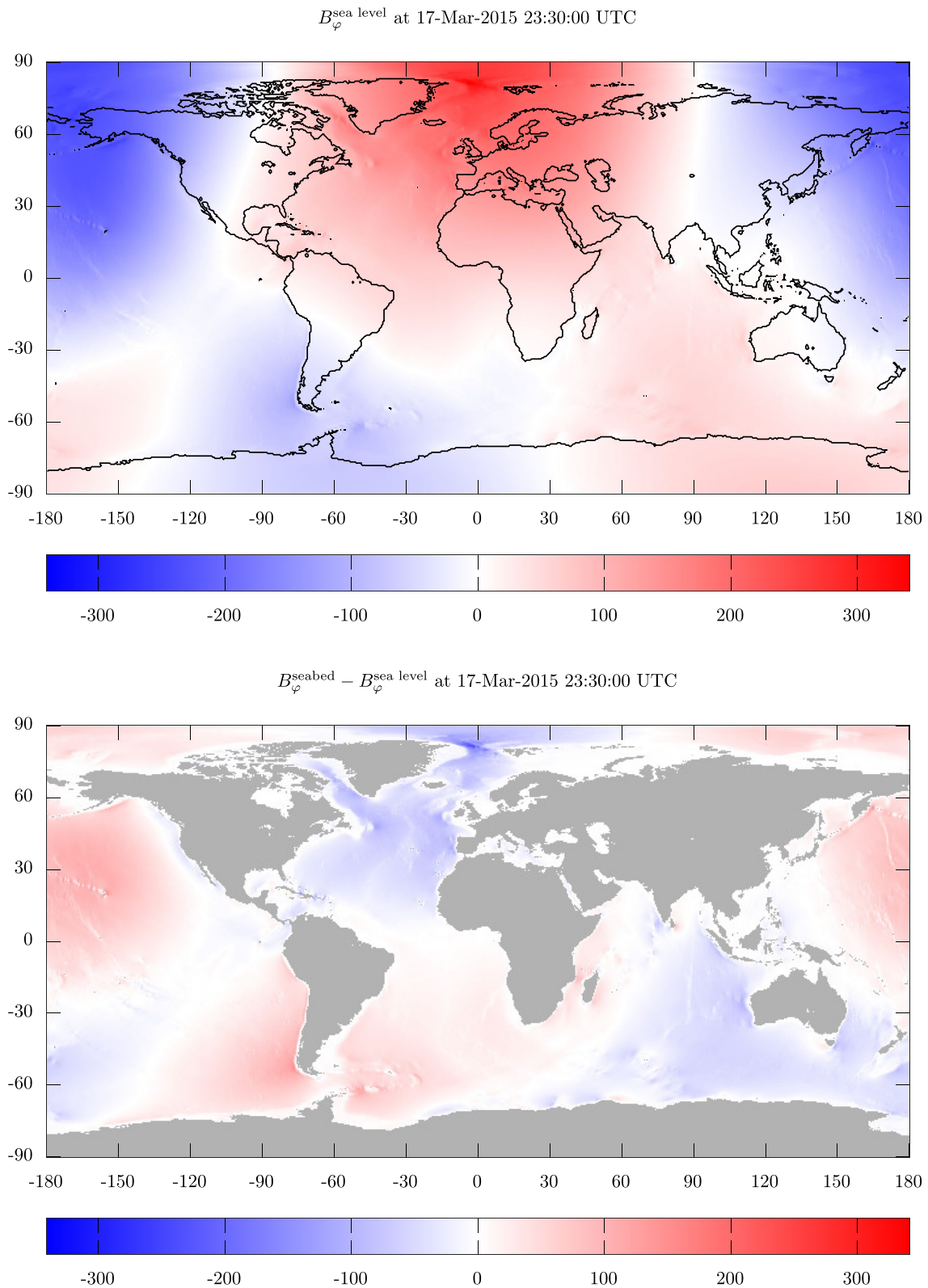$B_\theta^{\text{seabed}} - B_\theta^{\text{sea level}}$ at 17-Mar-2015 23:30:00 UTC

Figure 8. Modeled $B_\theta^{\text{sea level}}$ (top) and $B_\theta^{\text{seabed}} - B_\theta^{\text{sea level}}$ (bottom) at 23:30 17 March 2015 UTC (St. Patrick storm).The results are in nT.

$B_\varphi^{\text{sea level}}$ at 17-Mar-2015 23:30:00 UTC

$B_\varphi^{\text{seabed}} - B_\varphi^{\text{sea level}}$ at 17-Mar-2015 23:30:00 UTC

Figure 9. Modeled $B_\varphi^{\text{sea level}}$ (top) and $B_\varphi^{\text{seabed}} - B_\varphi^{\text{sea level}}$ (bottom) at 23:30 17 March 2015 UTC (St. Patrick storm). The results are in nT.

however, with visible dominance of spatial structure responsible for the symmetric part of the magnetospheric ring current.

4. Modeled Versus Observed Results

Now we compare storm-time time series of the modeled and observed magnetic fields in the region where we have both sea level (land-based) and seabed magnetic field measurements. From November 1999 to July 2000, the seabed magnetotelluric (MT) survey was conducted in the Philippine Sea (Seama et al., 2007) at six locations along a line at water depths between 3,250 and 5,430 m, depicted as OBEM 1, OBEM 2, …, OBEM 6 in Figure 10. Note that OBEM 3, which was installed on the seabed between sites OBEM 2 and OBEM 4, is not shown because it did not provide reliable data.

As for the land-based site, we have chosen the Kanoya (Intermagnet code: KNY) observatory, the nearest observatory to the seabed MT survey region. Figure 11 presents modeled and observed $\mathbf{B}_H$ at KNY and OBEM 1, OBEM 4, and OBEM 6 sites; OBEM 2 and OBEM 5 sites are excluded from the analysis not to overwhelm the exposition. Note that the baseline and a linear trend were subtracted from the data to remove core and crustal field contributions and possible instrument drift. We show the results for 4 days of the April 2000 storm, which appeared to be the only significant event during the deployment of the seabed MT instruments. We can make several observations from the figure: (a) modeled and observed results agree remarkably well for all (land-based and seabed) sites and both components; (b) an agreement is slightly better in B_θ which is three times larger than B_φ; (c) seabed signals at 20% smaller than land-based signals which is in agreement with the global results presented in the previous section.

However, during offshore drilling, no seabed magnetic field measurements are performed near the drilling site. Therefore, to correct magnetic field MWD for the disturbing effects from space-weather events (storms and substorms), one usually uses the magnetic field measurements from the adjacent land-based site/observatory, assuming that these signals are close to those one could observe at the seabed in the vicinity of the drilling site. But—as demonstrated in this and previous sections—land-based and seabed time-varying magnetic fields differ significantly. Considering this fact and encouraged by an agreement between modeled and observed results, we, in the next section, introduce a numerical scheme that allows researchers to obtain offshore seabed signals from the adjacent land-based observations.

5. Introducing a Numerical Scheme to Estimate Offshore Seabed Signals From the Adjacent Land-Based Observations

Let us imagine that the drilling is performed at an offshore (seabed) site $\mathbf{r}_{sb}$, and one has to estimate (and then account for) magnetic variations at $\mathbf{r}_{sb}$. A standard way to estimate these variations is to take magnetic field variations from the nearby land-based site $\mathbf{r}_{lb}$, assuming that variations at $\mathbf{r}_{sb}$ do not significantly differ from those at $\mathbf{r}_{lb}$. However, as we showed in Sections 3 and 4, horizontal components of the magnetic field are substantially different at sea level and seabed.

Below we propose and justify a scheme to more correctly estimate magnetic field variations at an offshore, that is, seabed, drilling point $\mathbf{r}_{sb}$. A scheme exploits an assumption that frequency-domain magnetic fields at locations $\mathbf{r}_{sb}$ and $\mathbf{r}_{lb}$ are related through inter-site 3×3 matrix transfer function T

$$\mathbf{B}\left(\mathbf{r}_{sb}, \omega; \sigma\right) \approx T\left(\mathbf{r}_{sb}, \mathbf{r}_{lb}, \omega; \sigma\right) \mathbf{B}\left(\mathbf{r}_{lb}, \omega; \sigma\right), \tag{14}$$

where

$$T\left(\mathbf{r}_{sb}, \mathbf{r}_{lb}, \omega; \sigma\right) = \begin{pmatrix} T_{rr} & T_{r\theta} & T_{r\varphi} \\ T_{\theta r} & T_{\theta\theta} & T_{\theta\varphi} \\ T_{\varphi r} & T_{\varphi\theta} & T_{\varphi\varphi} \end{pmatrix}. \tag{15}$$

It is important to stress that Equation 14 holds approximately, but as we will see later in this section, this approximation works well, especially when the lateral separation between land-based and seabed sites is not too large.
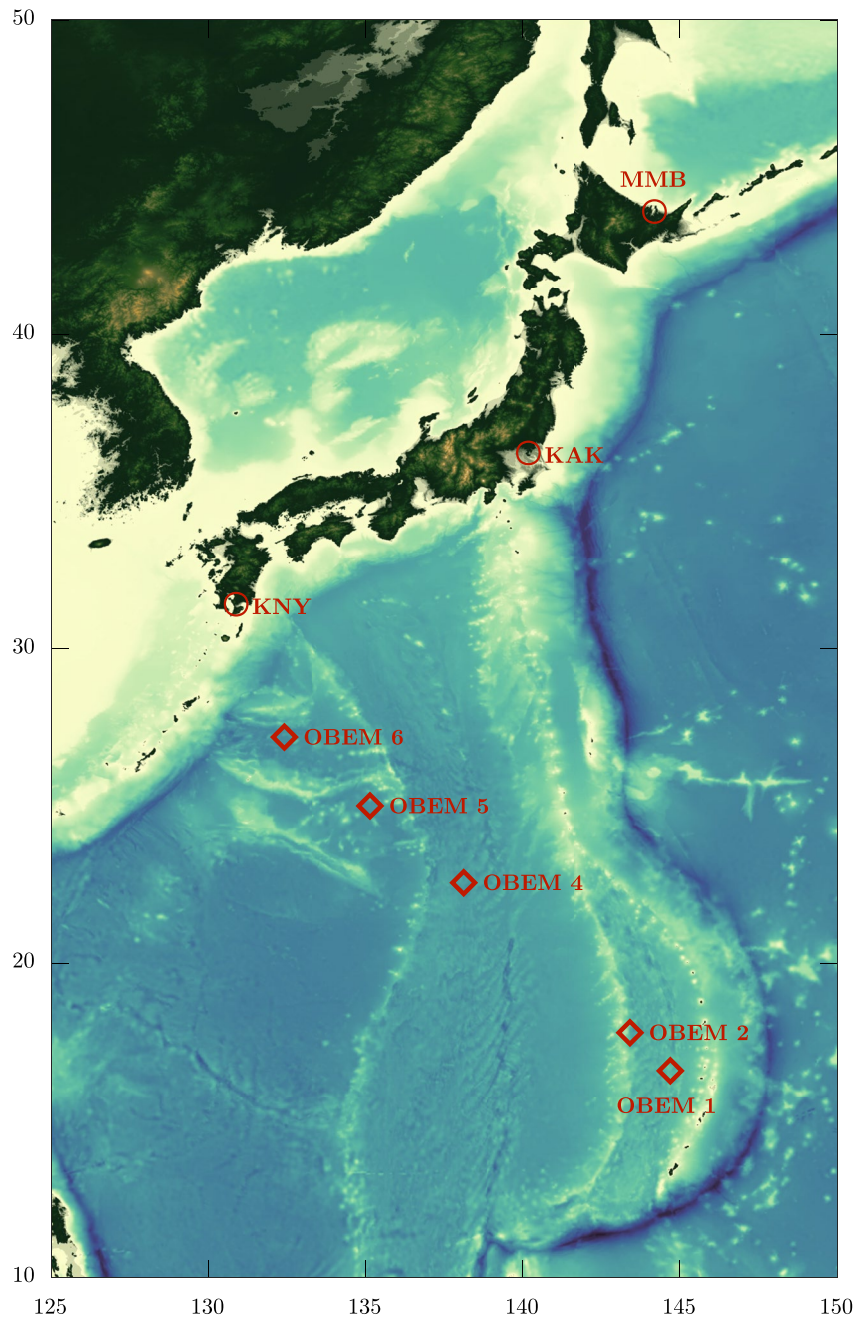
Figure 10. Locations of the land-based sites (Japanese geomagnetic observatories) and seabed sites. Note that OBEM 3, which was installed on the seabed between OBEM 2 and OBEM 4, did not provide useful data. Colors indicate topography/bathymetry.

Estimating the elements of T at a given frequency ω and conductivity model σ is performed as follows. First, one calculates the fields $\mathbf{B}_l^m(\mathbf{r}_{lb}, \omega; \sigma)$ and $\mathbf{B}_l^m(\mathbf{r}_{sb}, \omega; \sigma)$. Then, applying PCA to $\epsilon_l^m(t)$ one determines three dominant combinations of the $\mathbf{B}_l^m$ which we will denote as $\mathbf{B}^{(i)}$, $i = 1, 2, 3$ (see details in Appendix C). Finally, the elements of T are estimated row-wise using the $\mathbf{B}^{(i)}$ fields. For example, the elements of the first row of T are determined as the solution of the following SLE

$$T_{rr} B_r^{(i)}(\mathbf{r}_{lb}) + T_{r\theta} B_\theta^{(i)}(\mathbf{r}_{lb}) + T_{r\varphi} B_\varphi^{(i)}(\mathbf{r}_{lb}) = B_r^{(i)}(\mathbf{r}_{sb}), \ i = 1, 2, 3. \qquad (16)$$
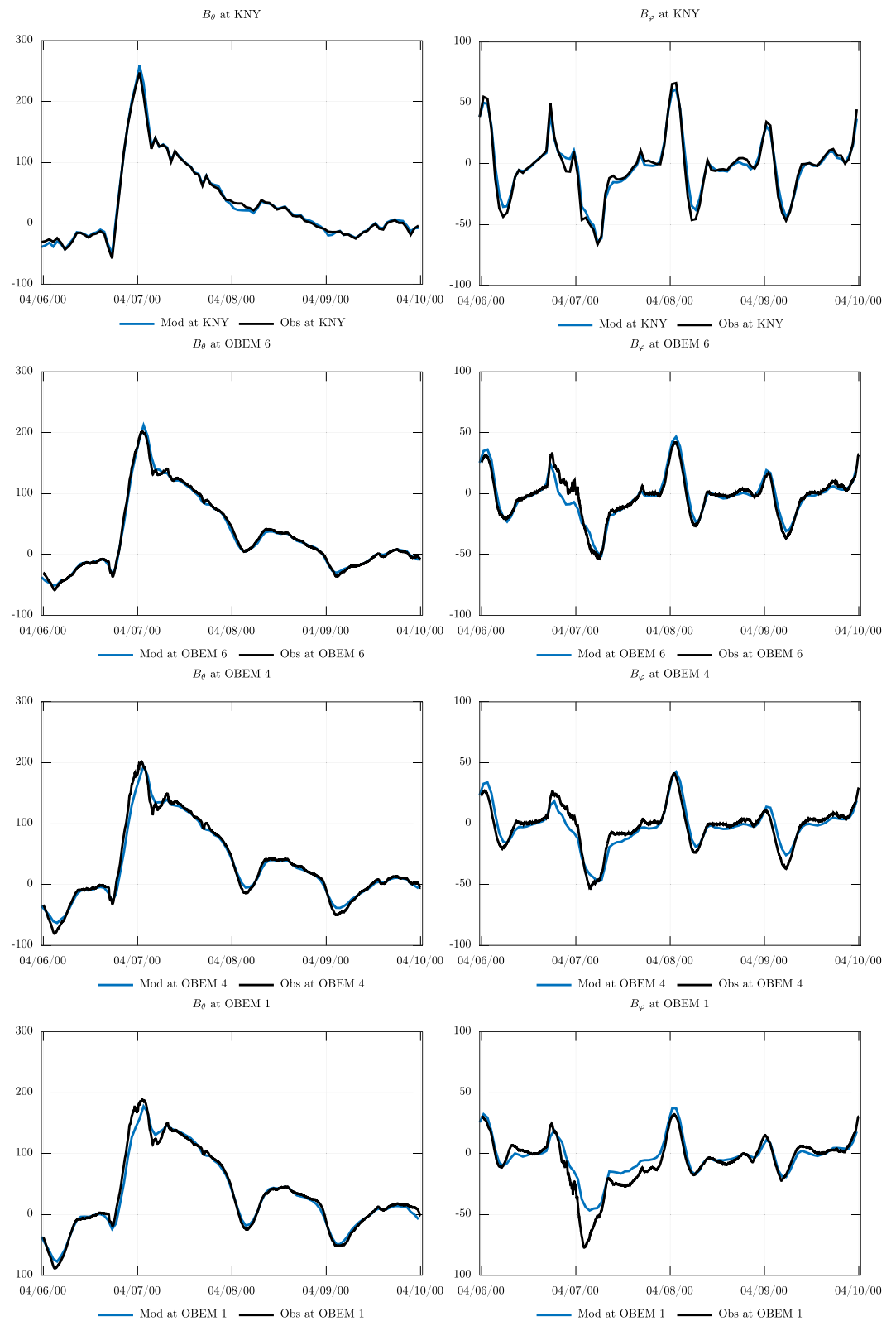
Figure 11. Modeled (blue) and observed (black) B_θ (left) and B_φ (right) at KNY and OBEM 1, OBEM 4, and OBEM 6 sites during 4–9 April 2000 storm. The results are in nT. Time is in UTC.

$B_r^{\text{sea level}}$ at 07-Apr-2000 00:30:00 UTC
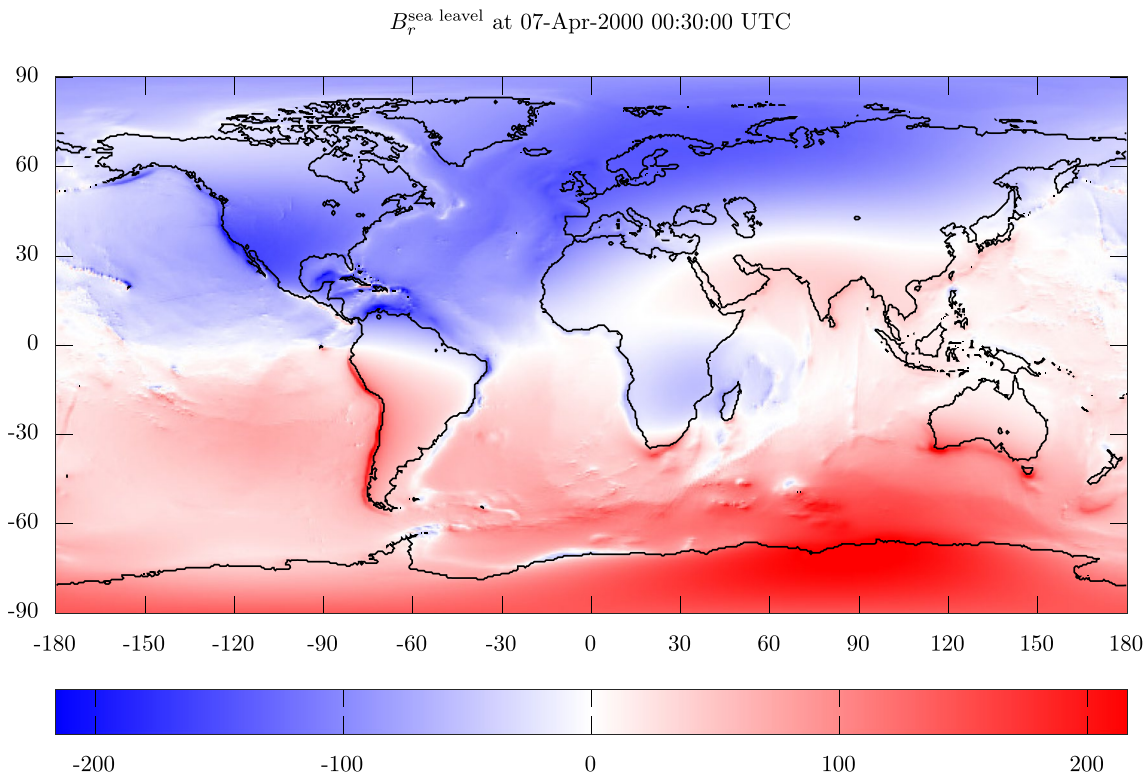
**Figure 12.** Modeled $B_r^{\text{sea level}}$ at 00:30 7 April 2000 UTC. The results are in nT.

Note, that in Equation 16 the dependency of all quantities on ω, $\mathbf{B}^{(i)}$ on σ, and elements of T on σ, $\mathbf{r}_{sb}$ and $\mathbf{r}_{lb}$ are omitted but implied. Once elements of T are estimated at a predefined frequencies, $\mathbf{B}$ at seabed site $\mathbf{r}_{sb}$ at a given time instant $t_k = k\Delta t$ is calculated similarly as it was done in Equation 11, that is,

$$\mathbf{B}\left(\mathbf{r}_{sb}, t_k; \sigma\right) \approx \sum_{n=0}^{N_t} \mathcal{T}^n\left(\mathbf{r}_{sb}, \mathbf{r}_{lb}, T; \sigma\right) \mathbf{B}\left(\mathbf{r}_{lb}, t_k - n\Delta t\right). \tag{17}$$

Before showing results justifying the proposed scheme, one critical comment is relevant here. In Section 3 we stated that the radial component (for the considered variations) is the same on the sea level and the seabed. Thus the question may arise why in Equation 14 we also invoke the radial components? To address this question, we remind the reader that the statement about the similarity of the radial component at sea level and the seabed is indeed valid, provided both signals refer to the same lateral location. However, in the problem setup we consider, the land-based (sea level) site is usually located at the coast and at a distance from the drilling point (as in our example). Moreover—and in contrast to horizontal components—the coastal radial field is dramatically distorted by the so-called ocean induction effect originating from large lateral conductivity contrasts between the ocean and land (Olsen & Kuvshinov, 2004; Parkinson & Jones, 1979). Figures 12–14 illustrates this fact by presenting a radial field at a global scale during the main phase of three storms mentioned above. One can see that, indeed, the magnitude of the radial component enhances substantially in coastal regions.

We calculated seabed fields using TF-based formalism discussed above and compared them with observations. As in Figure 11, Figure 15 shows results for 4 days of the April 2000 storm. It is seen that TF-based and observed results are in agreement with the observations at all three seabed sites and for both components. As expected, the agreement (generally very good) worsens with the distance from the land-based (KNY) site, which varies from 478 to 2,146 km (see Table 1). KNY results which are used in Equation 17 are also shown in the figure. Once again, one may notice that land-based results differ much from seabed results.

As a whole, Figure 15 demonstrates that, indeed, one can obtain trustworthy seabed signals by exploiting TF-based approach as applied to adjacent land-based measurements.

$B_r^{\text{sea level}}$ at 30-Oct-2003 20:30:00 UTC
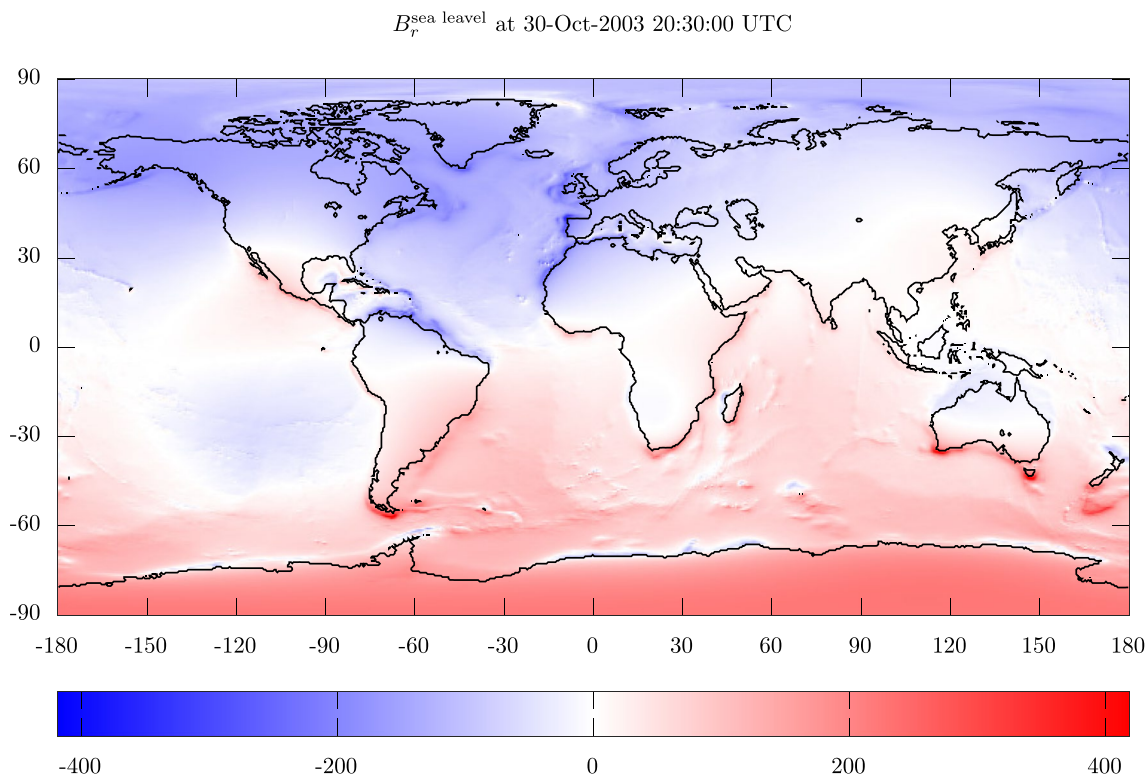
Figure 13. Modeled $B_r^{\text{sea level}}$ at 20:30 30 October 2003 UTC (Halloween storm). The results are in nT.

$B_r^{\text{sea level}}$ at 17-Mar-2015 23:30:00 UTC
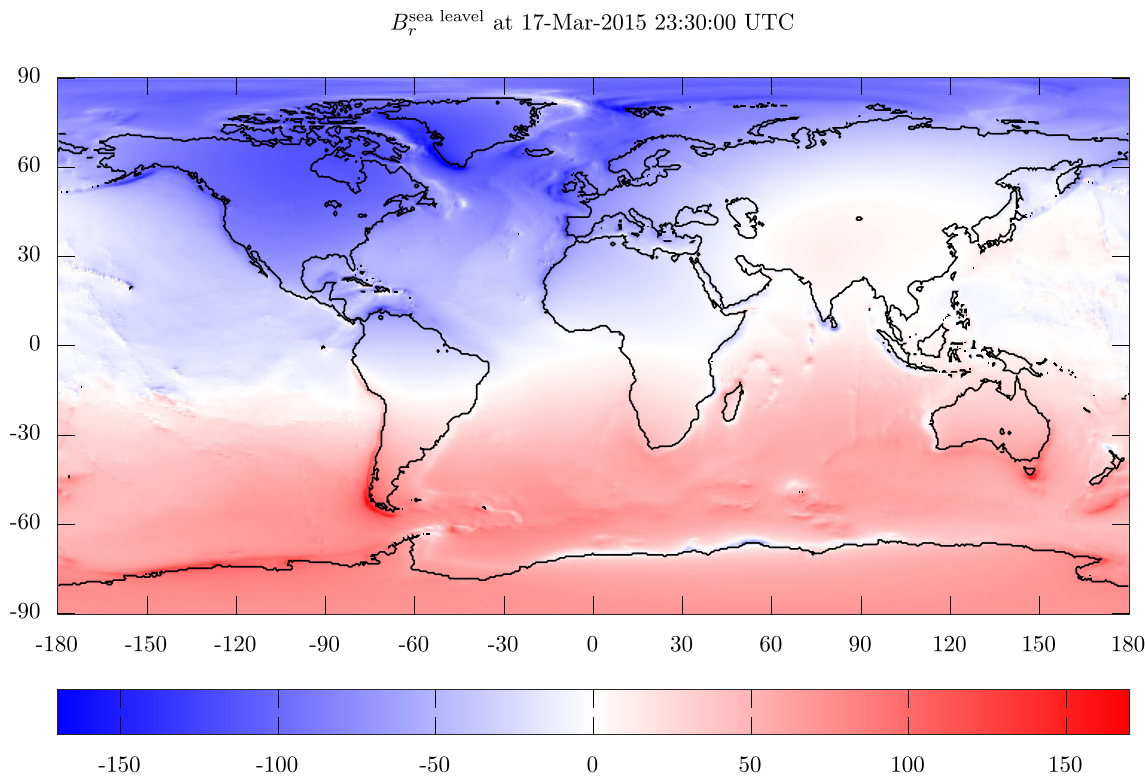
Figure 14. Modeled $B_r^{\text{sea level}}$ at 23:30 17 March 2015 UTC (St. Patrick storm). The results are in nT.
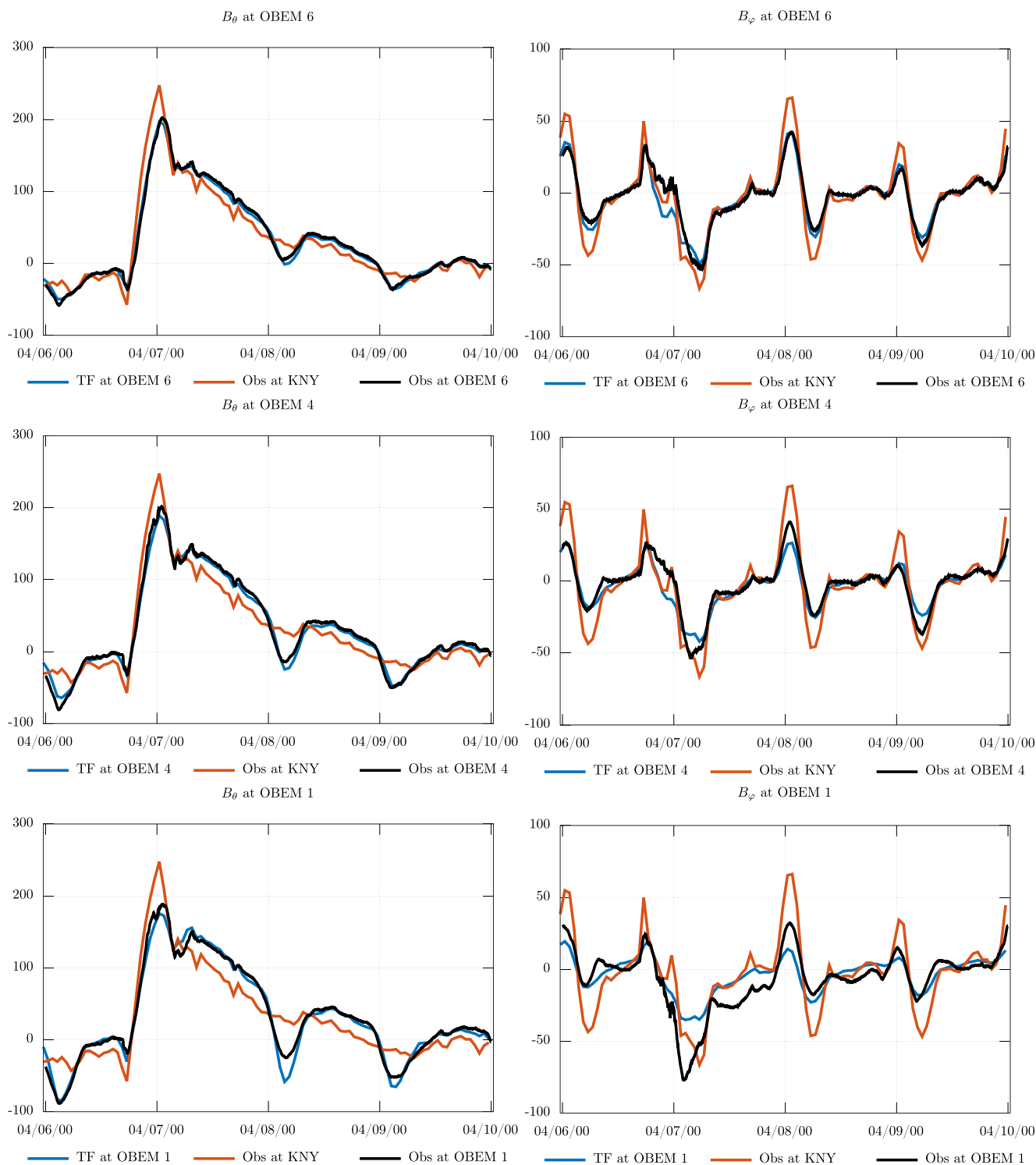
Figure 15. Modeled by transfer functions approach (blue) and observed (black) B_θ (left) and B_φ (right) at OBEM stations during 4–9 April 2000. Dark red stands for observed field components at Kanoya. The results are in nT. Time is in UTC.

6. Conclusions

In this paper, we presented an approach to efficiently calculating spatio-temporal evolution of magnetic field at any location (at satellite altitude, ground or seabed) in a given conductivity model of the Earth, provided the

Table 1
Coordinates of Seabed Sites, Their Depths, and Distances to Kanoya (KNY) Observatory

Site name	Latitude	Longitude	Depth (m)	Distance to KNY (km)
OBEM 1	16.573	144.695	3,259	2,146
OBEM 4	22.560	138.120	5,102	1,201
OBEM 6	27.190	132.417	5,431	478

source of magnetic field variations is also known. The approach relies on the factorization of the source by spatial modes and time series of respective expansion coefficients and exploits precomputed magnetic field kernels generated by corresponding spatial modes.

The methodology—being general—is implemented in this paper to model and analyze the spatio-temporal evolution of the magnetic field during geomagnetic storms. Global-scale problem setup advocates the parameterization of the magnetospheric source responsible for the storms using SH. We also presented a numerical scheme to estimate the time series of corresponding expansion coefficients using the data from the global network of geomagnetic observatories and exploiting precomputed magnetic field kernels.

We implemented the developed approach to model magnetic field behavior during three geomagnetic storms and demonstrated that the sea level horizontal magnetic fields significantly differ from those at the seabed, especially during the main phase of the geomagnetic storms. We then compared modeling results with observations at land-based and seabed sites and detected remarkable agreement between modeled and observed fields for all (land-based and seabed) sites and in both components.

Finally, we introduced and justified a scheme to obtain the seabed signals using the data from the adjacent land-based observatory and the results of comprehensive modeling. A method exploits a concept of transfer functions that relate—in frequency domain—three components of the magnetic field at the seabed site of interest with those at the land-based site. In an example of the seabed observations in the Philippine Sea, we demonstrate the workability of the proposed scheme.

This paper discussed magnetic fields induced by a large-scale magnetospheric source that dominates in mid- and low-latitudes. However, it is well known that one can expect much larger signals in polar regions due to substorm geomagnetic disturbances (Pirjola, 2002). The recovery of the spatio-temporal structure of the auroral ionospheric source, which is responsible for this activity, is more challenging due to the large variability of this source both in time and space. One of the ways to determine realistic auroral currents on a regional scale consists of collecting the data from high-latitude geomagnetic observatories and polar magnetometer arrays, for example, IMAGE array in Scandinavia (Tanskanen, 2009), CARISMA (Mann et al., 2008) and AUTUMNX (Connors et al., 2016) arrays in Canada, and then reconstructing the auroral current, for instance, by exploiting an approach based on spherical elementary current systems, SECS (Vanhamäki & Juusola, 2020). Note that this approach was used by Kruglyakov et al. (2022), who discussed real-time 3-D modeling of the ground electric field due to space weather events.

Once the auroral source is quantified, a similar numerical scheme described in the paper can be implemented with three modifications. One modification concerns the description of the substorm source—instead of using a SH representation, one can approximate the spatio-temporal evolution of the auroral ionospheric current via spatial modes obtained by PCA of SECS (Kruglyakov et al., 2022). Another modification applies to the 3-D conductivity model. Since substorm magnetic variations are characterized by periods between seconds and hours, one cannot exploit a model in which the surface layer is approximated by a thin shell, as this paper did. The variable thickness of this layer is essential in this period range; thus, a full 3-D model (including bathymetry) should be considered. The final modification invokes Cartesian geometry instead of the spherical geometry used in this paper. An application of the proposed scheme to a regional problem setup will be the subject of a subsequent publication.

Appendix A: Details of the Numerical Computation of Magnetic Field in Time Domain

In this section we provide details how equation

$$\mathbf{B}(\mathbf{r}_s, t; \sigma) = \sum_{l,m} \int_0^\infty \epsilon_l^m(t - \tau) \mathbf{B}_l^m(\mathbf{r}_s, \tau; \sigma) d\tau \approx \sum_{l,m} \int_0^T \epsilon_l^m(t - \tau) \mathbf{B}_l^m(\mathbf{r}_s, \tau; \sigma) d\tau, \qquad (A1)$$

in an assumption that ϵ_l^m are discrete time series with sampling interval Δt, is deduced to equation

$$\mathbf{B}\left(\mathbf{r}_s, t_k; \sigma\right) \approx \sum_{l,m} \sum_{n=0}^{N_t} \epsilon_l^m \left(t_k - n\Delta t\right) \mathcal{M}_{\mathbf{B}_l^m}^n \left(\mathbf{r}_s, T; \sigma\right), \tag{A2}$$

where t_k is a current time instant. First we notice that with finite T, one must account for a possibly non-negligible linear trend in time series $\epsilon_l^m(t)$. By removing the trend, we are forced to work with the following function

$$d_l^m(t, \tau; T) = \begin{cases} \epsilon_l^m(t - \tau) - \epsilon_l^m(t) - \dfrac{\epsilon_l^m(t - T) - \epsilon_l^m(t)}{T} \tau, & \tau \in [0, T] \\ 0, & \tau \notin [0, T]. \end{cases} \tag{A3}$$

Substituting Equation A3 into the right-hand side (RHS) of Equation A1, and considering (for simplicity) only one term in the sum, we obtain

$$\int_0^T \epsilon_l^m(t - \tau) \mathbf{B}_l^m\left(\mathbf{r}_s, \tau; \sigma\right) d\tau = \epsilon_l^m(t) \int_0^T \mathbf{B}_l^m\left(\mathbf{r}_s, \tau; \sigma\right) d\tau$$
$$+ \int_0^T d_l^m(t, \tau; T) \mathbf{B}_l^m\left(\mathbf{r}_s, \tau; \sigma\right) d\tau + \frac{\epsilon_l^m(t - T) - \epsilon_l^m(t)}{T} \int_0^T \tau \mathbf{B}_l^m\left(\mathbf{r}_s, \tau; \sigma\right) d\tau. \tag{A4}$$

Recall that T should be taken large enough to make approximation (A1) valid; particularly, this means that

$$\int_0^T \mathbf{B}_l^m\left(\mathbf{r}_s, \tau; \sigma\right) d\tau \approx \int_0^\infty \mathbf{B}_l^m\left(\mathbf{r}_s, \tau; \sigma\right) d\tau. \tag{A5}$$

Following Appendix A of Kruglyakov et al. (2022) the integral in the RHS of the latter equation can be expressed as

$$\int_0^\infty \mathbf{B}_l^m\left(\mathbf{r}_s, \tau; \sigma\right) d\tau = \lim_{T \to \infty} \frac{2}{\pi} \int_0^T \left[\int_0^\infty \operatorname{Re} \mathbf{B}_l^m\left(\mathbf{r}_s, \omega; \sigma\right) \cos(\omega\tau) d\omega \right] d\tau =$$
$$\lim_{T \to \infty} \frac{2}{\pi} \int_0^\infty \operatorname{Re} \mathbf{B}_l^m\left(\mathbf{r}_s, \omega; \sigma\right) \frac{\sin(\omega T)}{\omega} d\omega = \left. \operatorname{Re} \mathbf{B}_l^m\left(\mathbf{r}_s, \omega; \sigma\right) \right|_{\omega=0}. \tag{A6}$$

Then, Equation A4 can be approximated as

$$\int_0^T \epsilon_l^m(t - \tau) \mathbf{B}_l^m\left(\mathbf{r}_s, \tau; \sigma\right) d\tau \approx \epsilon_l^m(t) \left. \operatorname{Re} \mathbf{B}_l^m\left(\mathbf{r}_s, \omega; \sigma\right) \right|_{\omega=0}$$
$$+ \int_0^T d_l^m(t, \tau; T) \mathbf{B}_l^m\left(\mathbf{r}_s, \tau; \sigma\right) d\tau$$
$$+ \left[\epsilon_l^m(t - T) - \epsilon_l^m(t) \right] \mathcal{L}_l^m\left(\mathbf{r}_s, T; \sigma\right), \tag{A7}$$

where

$$\mathcal{L}_l^m\left(\mathbf{r}_s, T; \sigma\right) = \frac{1}{T} \int_0^T \tau \mathbf{B}_l^m\left(\mathbf{r}_s, \tau; \sigma\right) d\tau. \tag{A8}$$

The integrals $\mathcal{L}_l^m\left(\mathbf{r}_s, T; \sigma\right)$ can be computed using the digital filter technique (see Appendix B), whereas second term in the RHS of Equation A7 is estimated as follows.

Taking into account that we have $\epsilon_l^m(t)$ at discrete time instants, $t = n\Delta t$, $n = 0, 1, \ldots$, we approximate $d_l^m(t, \tau; T)$ using the Whittaker-Shannon (sinc) interpolation formula

$$d_l^m(t, \tau; T) \approx \sum_{n=0}^{n\Delta t \leq T} d_l^m(t, n\Delta t; T) \operatorname{sinc} \frac{\tau - n\Delta t}{\Delta t}, \tag{A9}$$

where

$$\text{sinc}(x) = \frac{\sin \pi x}{\pi x}. \tag{A10}$$

Recall that sinc interpolation is a method to construct a continuous band-limited function from a sequence of real numbers, in our case time series d_l^m at time instants $t = n\Delta t$, $n = 0, 1, \dots$. Note that in our context, the term "band-limited function" means that non-zero values of a Fourier transform of this function are confined to the frequencies

$$|\omega| \leq \frac{\pi}{\Delta t}. \tag{A11}$$

Using the approximation (A9) and taking into account that $\mathbf{B}_l^m(\mathbf{r}_s, \tau; \sigma) = 0$, $\tau < 0$ (see Appendix A of Kruglyakov et al. (2022)), one obtains

$$\int_0^T d_l^m(t, \tau; T)\mathbf{B}_l^m(\mathbf{r}_s, \tau; \sigma)\, d\tau \approx \int_0^\infty d_l^m(t, \tau; T)\mathbf{B}_l^m(\mathbf{r}_s, \tau; \sigma)\, d\tau = \tag{A12}$$

$$\int_{-\infty}^\infty d_l^m(t, \tau; T)\mathbf{B}_l^m(\mathbf{r}_s, \tau; \sigma)\, d\tau = \sum_{n=0}^{n\Delta t \leq T} d_l^m(t, n\Delta t; T)\int_{-\infty}^\infty \mathbf{B}_l^m(\mathbf{r}_s, \tau; \sigma)\, \text{sinc}\frac{\tau - n\Delta t}{\Delta t}\, d\tau.$$

Thus, we can write

$$\int_0^T d_l^m(t, \tau; T)\mathbf{B}_l^m(\mathbf{r}_s, \tau; \sigma)\, d\tau = \sum_{n=0}^{n\Delta t \leq T} d_l^m(t, n\Delta t; T)\widetilde{\mathcal{M}}_{\mathbf{B}_l^m}^n(\mathbf{r}_s; \sigma), \tag{A13}$$

where

$$\widetilde{\mathcal{M}}_{\mathbf{B}_l^m}^n(\mathbf{r}_s; \sigma) = \int_{-\infty}^\infty \mathbf{B}_l^m(\mathbf{r}_s, \tau; \sigma)\, \text{sinc}\frac{\tau - n\Delta t}{\Delta t}\, d\tau. \tag{A14}$$

Further, following the properties of the Fourier transform as applied to sinc function, we obtain that

$$\widetilde{\mathcal{M}}_{\mathbf{B}_l^m}^n(\mathbf{r}_s; \sigma) = \frac{\Delta t}{2\pi}\int_{-\frac{\pi}{\Delta t}}^{\frac{\pi}{\Delta t}} \mathbf{B}_l^m(\mathbf{r}_s, \omega; \sigma)\, e^{-i\omega n\Delta t}\, d\omega = \text{Re}\left\{\frac{\Delta t}{\pi}\int_0^{\frac{\pi}{\Delta t}} \mathbf{B}_l^m(\mathbf{r}_s, \omega; \sigma)\, e^{-i\omega n\Delta t}\, d\omega\right\}. \tag{A15}$$

Finally, substituting Equation A13 in Equation A7, and Equation A7 in the RHS of Equation A1 we obtain

$$\mathbf{B}(\mathbf{r}_s, t_k; \sigma) \approx \sum_{l,m}\left\{\epsilon_l^m(t)\, \text{Re}\, \mathbf{B}_l^m(\mathbf{r}_s, \omega; \sigma)\big|_{\omega=0} + \sum_{n=0}^{N_t} d_l^m(t_k, n\Delta t; T)\widetilde{\mathcal{M}}_{\mathbf{B}_l^m}^n(\mathbf{r}_s; \sigma)\right.$$
$$\left. + \left[\epsilon_l^m(t_k - T) - \epsilon_l^m(t_k)\right]\mathcal{L}_l^m(\mathbf{r}_s, T; \sigma)\right\}.$$

The latter equation can be written in the form of Equation A2 where

$$\mathcal{M}_{\mathbf{B}_l^m}^n(\mathbf{r}_s, T; \sigma) = \begin{cases} \text{Re}\, \mathbf{B}_l^m(\mathbf{r}_s, \omega; \sigma)\big|_{\omega=0} - \mathcal{L}_l^m(\mathbf{r}_s, T; \sigma) - \sum_{k=1}^{N_t-1}\widetilde{\mathcal{M}}_{\mathbf{B}_l^m}^k(\mathbf{r}_s; \sigma)\left(1 - \frac{k}{N_t}\right), & n = 0 \\ \widetilde{\mathcal{M}}_{\mathbf{B}_l^m}^n(\mathbf{r}_s; \sigma), & n = 1, 2, \dots, N_t - 1 \\ \mathcal{L}_l^m(\mathbf{r}_s, T; \sigma) - \sum_{k=1}^{N_t-1}\widetilde{\mathcal{M}}_{\mathbf{B}_l^m}^k(\mathbf{r}_s; \sigma)\frac{k}{N_t}, & n = N_t \end{cases} \tag{A16}$$

and where $\mathcal{L}_l^m(\mathbf{r}_s, T; \sigma)$, and $\widetilde{\mathcal{M}}_{\mathbf{B}_l^m}^n(\mathbf{r}_s; \sigma)$ are defined in Equations A8 and A15, respectively.

Computation of the integrals in the RHS of Equation A15 is performed as follows. First, $\mathbf{B}_l^m(\mathbf{r}_s, \omega; \sigma)$ are computed at zero frequency and at 43 logarithmically spaced frequencies between $1/\Delta t$ and $1/(10^7 \Delta t)$, where Δt is one hour for our problem setup. Further, using cubic spline interpolation as applied to calculated $\mathbf{B}_l^m(\mathbf{r}_s, \omega; \sigma)$, one can analytically compute integrals in the RHS of Equation A15.

An important note here is that, according to Equation A15, one does not need to compute $\mathbf{B}_l^m(\mathbf{r}_s, \omega; \sigma)$ for $\omega > \frac{\pi}{\Delta t}$ (corresponding to the period $P = 2\Delta t$). This may be obvious, however, this is not the case if one uses piece-wise constant (PWC) approximation of $\epsilon_l^m(t)$ as it is done, for example, in Grayver et al. (2021). With PWC approximation, one is forced to compute the fields at very high frequencies irrespective of Δt value; this can pose a problem from the numerical point of view.

Appendix B: Computation of $\mathcal{L}_l^m(\mathbf{r}_s, T; \sigma)$

Since $\mathbf{B}_l^m(\mathbf{r}_s, \tau; \sigma)$ is real-valued and causal, it can be written as (cf. Appendix A of Kruglyakov et al. (2022))

$$\mathbf{B}_l^m(\mathbf{r}_s, \tau; \sigma) = \frac{2}{\pi} \int_0^\infty \operatorname{Im} \mathbf{B}_l^m(\mathbf{r}_s, \omega; \sigma) \sin(\omega\tau)\, d\omega. \tag{B1}$$

Substituting the latter equation into Equation A8 and rearranging the order of integration, we write $\mathcal{L}_l^m(\mathbf{r}_s, T; \sigma)$ in the following form

$$\mathcal{L}_l^m(\mathbf{r}_s, T; \sigma) = T \int_0^\infty \Phi(\omega T) \operatorname{Im} \mathbf{B}_l^m(\mathbf{r}_s, \omega; \sigma)\, d\omega, \tag{B2}$$

where $\Phi(\omega T)$ reads

$$\Phi(\omega T) = \frac{2}{\pi} \frac{1}{T^2} \int_0^T \tau \sin(\omega\tau) d\tau = \frac{2}{\pi} \left[\frac{\sin(\omega T)}{(\omega T)^2} - \frac{\cos(\omega T)}{\omega T} \right]. \tag{B3}$$

Integrals in Equation B2 can be efficiently estimated using the digital filter technique. Specifically, one needs to construct a digital filter for the following integral transform

$$F(T) = T \int_0^\infty \Phi(\omega T) f(\omega) d\omega. \tag{B4}$$

To obtain filter's coefficients for this transform, we exploit the same procedure as in Werthmüller et al. (2019) using the following pair of output and input functions

$$\begin{aligned} F(T) &= \frac{(T+1)e^{-T} - 1}{T}, \\ f(\omega) &= \frac{\omega}{1 + \omega^2}. \end{aligned} \tag{B5}$$

Appendix C: Obtaining $\mathbf{B}^{(i)}$, $i = 1, 2, 3$

Here we present a scheme to obtain $\mathbf{B}^{(i)}$, $i = 1, 2, 3$ thus allowing us to calculate the desired inter-site transfer function (cf. Equation 14). Specifically, the scheme includes the following steps:

1. We estimate $N_c = 24$ times series $\epsilon_l^m(t)$ as in Section 3.2
2. We perform principal component analysis of these time series to obtain three "major modes" with time series $\nu_i(t)$, $i = 1, 2, 3$ and 3×24 (time independent) matrix $\mathcal{D}$ to express new series in terms of the old ones

$$\nu_i(t) = \sum_{l,m} \mathcal{D}_i^{l,m} \epsilon_l^m(t), i = 1, 2, 3. \tag{C1}$$

3. We apply matrix $\mathcal{D}$ to $\mathbf{B}_l^m$ (both in time and frequency domain) to obtain fields $\mathbf{B}^{(i)}$ corresponding to $\nu_i(t)$, $i = 1$, 2, 3 as

$$\mathbf{B}^{(i)}(\mathbf{r}, t; \sigma) = \sum_{l,m} \mathcal{D}_i^{l,m} \mathbf{B}_l^m(\mathbf{r}, t; \sigma),$$

$$\mathbf{B}^{(i)}(\mathbf{r}, \omega; \sigma) = \sum_{l,m} \mathcal{D}_i^{l,m} \mathbf{B}_l^m(\mathbf{r}, \omega; \sigma).$$

(C2)

Data Availability Statement

- The global map of ocean and sediments conductance by Grayver (2021) is available at https://doi.org/10.5281/zenodo.7224268 (The mirror of the original map from https://github.com/agrayver/seasigma at Zenodo).
- The global conductivity model by Alekseev et al. (2015) is available at https://globalconductivity.ocean.ru/downloads.html.
- The conductivity model for North America by Kelbert et al. (2019) is available at http://ds.iris.edu/ds/products/emc-conus-mt-2021/.
- 1-D global conductivity model is published in a form of Table 1 in Kuvshinov et al. (2021).
- Solver GEMMIE (Kruglyakov & Kuvshinov, 2022) is available at https://gitlab.com/m.kruglyakov/gemmie under GPL v2 license.
- The data of the ocean bottom survey is available at http://ohpdmc.eri.u-tokyo.ac.jp/dataset/campaign/obem/phs99-00/data/index.html.
- The cleaned magnetic field data based on measurements from the global (INTERMAGNET) network of observatories are available by following the instructions at https://notebooks.vires.services/notebooks/04c2_geomag-ground-data-vires.

References

Alekseev, D., Kuvshinov, A., & Palshin, N. (2015). Compilation of 3-D global conductivity model of the Earth for space weather applications. *Earth Planets and Space*, *67*(1), 108–118. https://doi.org/10.1186/s40623-015-0272-5

Beggan, C. D., Macmillan, S., Brown, W. J., & Grindrod, S. J. (2021). Quantifying global and random uncertainties in high resolution global geomagnetic field models used for directional drilling. *SPE Drilling and Completion*, *36*(03), 603–612. https://doi.org/10.2118/204038-PA

Buchanan, A., Finn, C., Love, J. J., Worthington, E. W., Lawson, F., Maus, S., et al. (2013). Geomagnetic referencing—The real-time compass for directional drillers. *Oilfield Review*, *25*(3), 32–47.

Connors, M., Schofield, I., Reiter, K., Chi, P. J., Rowe, K. M., & Russell, C. T. (2016). The AUTUMNX magnetometer meridian chain in Québec, Canada. *Earth Planets and Space*, *68*(1), 2. https://doi.org/10.1186/s40623-015-0354-4

Egbert, G. D., Alken, P., Maute, A., Zhang, H., & Richmond, A. D. (2021). Modeling diurnal variation magnetic fields for mantle induction studies. *Geophysical Journal International*, *225*(2), 1086–1109. https://doi.org/10.1093/gji/ggaa533

Finlay, C., Kloss, C., Olsen, N., Hammer, M., Toffner-Clausen, L., Grayver, A., & Kuvshinov, A. (2020). The CHAOS-7 geomagnetic field model and observed changes in the South Atlantic Anomaly. *Earth Planets and Space*, *72*(1), 156. https://doi.org/10.1186/s40623-020-01252-9

Grayver, A. (2021). Global 3-D electrical conductivity model of the world ocean and marine sediments. *Geochemistry, Geophysics, Geosystems*, *22*(9), e2021GC009950. https://doi.org/10.1029/2021GC009950

Grayver, A., Kuvshinov, A., & Werthmüller, D. (2021). Time-domain modeling of 3-D Earth's and planetary electromagnetic induction effect in ground and satellite observations. *Journal of Geophysical Research: Space Physics*, *126*(3), e2020JA028672. https://doi.org/10.1029/2020JA028672

Guzavina, M., Grayver, A., & Kuvshinov, A. (2019). Probing upper mantle electrical conductivity with daily magnetic variations using global to local transfer functions. *Geophysical Journal International*, *219*(3), 2125–2147. https://doi.org/10.1093/gji/ggz412

Honkonen, I., Kuvshinov, A., Rastätter, L., & Pulkkinen, A. (2018). Predicting global ground geoelectric field with coupled geospace and three-dimensional geomagnetic induction models. *Space Weather*, *16*(8), 1028–1041. https://doi.org/10.1029/2018SW001859

Ivannikova, E., Kruglyakov, M., Kuvshinov, A., Rastätter, L., & Pulkkinen, A. (2018). Regional 3-D modeling of ground electromagnetic field due to realistic geomagnetic disturbances. *Space Weather*, *16*(5), 476–500. https://doi.org/10.1002/2017SW001793

Kelbert, A., Bedrosian, P., & Murphy, B. (2019). The first 3D conductivity model of the contiguous US: Reflections on geologic structure and application to induction hazards. In J. Gannon, Z. Xu, & A. Swidinski (Eds.), *Geomagnetically induced currents from the sun to the power grid*. American Geophysical Union. https://doi.org/10.1102/9781119434412

Kruglyakov, M., & Kuvshinov, A. (2022). Modelling tippers on a sphere. *Geophysical Journal International*, *231*(2), 737–748. https://doi.org/10.1093/gji/ggac199

Kruglyakov, M., Kuvshinov, A., & Marshalko, E. (2022). Real-Time 3-D Modeling of the Ground Electric Field Due To Space Weather Events. A Concept and Its Validation. *Space Weather*, *20*(4). https://doi.org/10.1029/2021sw002906

Kuvshinov, A. (2008). 3-D global induction in the oceans and solid Earth: Recent progress in modeling magnetic and electric fields from sources of magnetospheric, ionospheric and oceanic origin. *Surveys in Geophysics*, *29*(2), 139–186. https://doi.org/10.1007/s10712-008-9045-z

Kuvshinov, A., Grayver, A., Toffner-Clausen, L., & Olsen, N. (2021). Probing 3-D electrical conductivity of the mantle using 6 years of Swarm, CryoSat-2 and observatory magnetic data and exploiting matrix Q-responses approach. *Earth Planets and Space*, *73*(1), 67. https://doi.org/10.1186/s40623-020-01341-9

Macmillan, S., & Olsen, N. (2013). Observatory data and the Swarm mission. *Earth Planets and Space*, *65*(11), 1355–1362. https://doi.org/10.5047/eps.2013.07.011

Mann, I. R., Milling, D. K., Rae, I. J., Ozeke, L. G., Kale, Z. C., Murphy, K. R., et al. (2008). The upgraded CARISMA magnetometer array in the THEMIS era. *Space Science Reviews*, *141*(1), 413–451. https://doi.org/10.1007/s11214-008-9457-6

Nair, M., Chulliat, A., Woods, A., Alken, P., Meyer, B., Poedjono, B., et al. (2021). Next generation high-definition geomagnetic model for wellbore positioning, incorporating new crustal magnetic data (Vol. *4*). https://doi.org/10.4043/31044-MS

Olsen, N., & Kuvshinov, A. (2004). Modelling the ocean effect of geomagnetic storms. *Earth Planets and Space*, *56*(5), 525–530. https://doi.org/10.1186/bf03352512

Pankratov, O., & Kuvshinov, A. (2016). Applied mathematics in EM studies with special emphasis on an uncertainty quantification and 3-D integral equation modelling. *Surveys in Geophysics*, *37*(1), 109–147. https://doi.org/10.1007/s10712-015-9340-4

Parkinson, W. D., & Jones, F. W. (1979). The geomagnetic coast effect. *Reviews of Geophysics*, *17*(8), 1999–2015. https://doi.org/10.1029/rg017i008p01999

Pirjola, R. (2002). Review on the calculation of surface electric and magnetic fields and of geomagnetically induced currents in ground-based technological systems. *Surveys in Geophysics*, *23*, 71–90.

Poedjono, B., Pai, S., Maus, S., Manoj, C., & Paynter, R. (2015). Using autonomous marine vehicles to enable accurate wellbore placement in the Arctic. https://doi.org/10.4043/25545-MS

Püthe, C., & Kuvshinov, A. (2013). Towards quantitative assessment of the hazard from space weather. Global 3-D modellings of the electric field induced by a realistic geomagnetic storm. *Earth Planets and Space*, *65*(9), 1017–1025. https://doi.org/10.5047/eps.2013.03.003

Reay, S., Allen, W., Baillie, O., Bowe, J., Clarke, E., Lesur, V., & Macmillan, S. (2005). Space weather effects on drilling accuracy in the North Sea. *Annales Geophysicae*, *23*(9), 3081–3088. https://doi.org/10.5194/angeo-23-3081-2005

Seama, N., Baba, K., Utada, H., Toh, H., Tada, N., Ichiki, M., & Matsuno, T. (2007). 1-D electrical conductivity structure beneath the Philippine Sea: Results from an ocean bottom magnetotelluric survey. *Physics of the Earth and Planetary Interiors*, *162*(1–2), 2–12. https://doi.org/10.1016/j.pepi.2007.02.014

Sun, J., & Egbert, G. D. (2012). Spherical decomposition of electromagnetic fields generated by quasi-static currents. *GEM—International Journal on Geomathematics*, *3*(2), 279–295. https://doi.org/10.1007/s13137-012-0039-0

Tanskanen, E. I. (2009). A comprehensive high-throughput analysis of substorms observed by IMAGE magnetometer network: Years 1993–2003 examined. *Journal of Geophysical Research*, *114*(A5), A05204. https://doi.org/10.1029/2008JA013682

Vanhamäki, H., & Juusola, L. (2020). Introduction to spherical elementary current systems. In M. W. Dunlop & H. Lühr (Eds.), *Ionospheric multi-spacecraft analysis tools: Approaches for deriving ionospheric parameters* (pp. 5–33). Springer International Publishing. https://doi.org/10.1007/978-3-030-26732-2_2

Werthmüller, D., Key, K., & Slob, E. C. (2019). A tool for designing digital filters for the Hankel and Fourier transforms in potential, diffusive, and wavefield modeling. *Geophysics*, *84*(2), F47–F56. https://doi.org/10.1190/geo2018-0069.1

Zenhausern, G., Kuvshinov, A., Guzavina, M., & Maute, A. (2021). Towards probing Earth's upper mantle with daily magnetic field variations: Exploring a physics-based parametrization of the source. *Earth Planets and Space*, *73*(1), 136. https://doi.org/10.1186/s40623-021-01455-8